

Contents lists available at ScienceDirect

Petroleum Science

journal homepage: www.keaipublishing.com/en/journals/petroleum-science



Original Paper

A multi-scale and multi-mechanism coupled model for carbon isotope fractionation of methane during shale gas production



Jun Wang ^a, Fang-Wen Chen ^{a, c}, Wen-Biao Li ^{b, d, e, *}, Shuang-Fang Lu ^{b, c, d, e, **}, Sheng-Xian Zhao ^f, Yong-Yang Liu ^f, Zi-Yi Wang ^a

- ^a School of Geosciences, China University of Petroleum (East China), Qingdao, 266580, Shandong, China
- ^b Sanya Offshore Oil & Gas Research Institute of Northeast Petroleum University, Sanya, 572025, Hainan, China
- ^c Key Laboratory of Deep Oil and Gas, China University of Petroleum (East China), Qingdao, 266580, Shandong, China
- ^d National Key Laboratory of Continental Shale Oil, Northeast Petroleum University, Daqing, 163318, Heilongjiang, China
- ^e Key Laboratory of Continental Shale Hydrocarbon Accumulation and Efficient Development, Ministry of Education, Northeast Petroleum University, Daging, 163318, Heilongjiang, China
- f Shale Gas Institute of PetroChina Southwest Oil & Gasfield Company, Chengdu, 610000, Sichuan, China

ARTICLE INFO

Article history: Received 20 June 2024 Received in revised form 2 December 2024 Accepted 24 March 2025 Available online 26 March 2025

Edited by Jie Hao and Min Li

Keywords: Shale gas Isotope fractionation Multi-scale Production prediction Adsorbed/free gas ratio

ABSTRACT

Prediction of production decline and evaluation of the adsorbed/free gas ratio are critical for determining the lifespan and production status of shale gas wells. Traditional production prediction methods have some shortcomings because of the low permeability and tightness of shale, complex gas flow behavior of multi-scale gas transport regions and multiple gas transport mechanism superpositions, and complex and variable production regimes of shale gas wells. Recent research has demonstrated the existence of a multi-stage isotope fractionation phenomenon during shale gas production, with the fractionation characteristics of each stage associated with the pore structure, gas in place (GIP), adsorption/desorption, and gas production process. This study presents a new approach for estimating shale gas well production and evaluating the adsorbed/free gas ratio throughout production using isotope fractionation techniques. A reservoir-scale carbon isotope fractionation (CIF) model applicable to the production process of shale gas wells was developed for the first time in this research. In contrast to the traditional model, this model improves production prediction accuracy by simultaneously fitting the gas production rate and $\delta^{13}C_1$ data and provides a new evaluation method of the adsorbed/free gas ratio during shale gas production. The results indicate that the diffusion and adsorption/desorption properties of rock, bottom-hole flowing pressure (BHP) of gas well, and multi-scale gas transport regions of the reservoir all affect isotope fractionation, with the diffusion and adsorption/desorption parameters of rock having the greatest effect on isotope fractionation being D^*/D , P_1 , V_1 , α , and others in that order. We effectively tested the universality of the four-stage isotope fractionation feature and revealed a unique isotope fractionation mechanism caused by the superimposed coupling of multi-scale gas transport regions during shale gas well production. Finally, we applied the established CIF model to a shale gas well in the Sichuan Basin, China, and calculated the estimated ultimate recovery (EUR) of the well to be 3.33×10^8 m³; the adsorbed gas ratio during shale gas production was 1.65%, 10.03%, and 23.44% in the first, fifth, and tenth years, respectively. The findings are significant for understanding the isotope fractionation mechanism during natural gas transport in complex systems and for formulating and optimizing unconventional natural gas development strategies.

© 2025 The Authors. Publishing services by Elsevier B.V. on behalf of KeAi Communications Co. Ltd. This is an open access article under the CC BY-NC-ND license (http://creativecommons.org/licenses/by-nc-nd/

4.0/).

1. Introduction

Shale gas has become a hotspot for exploration and development because of its widespread distribution, large resource reserves, and environmentally friendly characteristics. In terms of

^{*} Corresponding author.

^{**} Corresponding author.

E-mail addresses: liwenbiao1996nepu@163.com (W.-B. Li), lushuangfang@nepu.
edu.cn (S.-F. Lu).

commercial exploitation, North America, Canada, and China have taken the lead globally (IEA, 2016). However, many challenges remain to be explored and solved. Production forecasting and the evaluation of the adsorbed/free gas ratio (the ratio of the absorbed/free gas production rate to the total gas production rate) during shale gas well production are related to the development and optimization of production strategies for shale gas wells, thus attracting the interest of academia and industry.

There are numerous techniques for predicting shale gas production. The currently available methods can be categorized into three groups: production decline analysis methods, analytical solution methods, and numerical simulation methods. The production decline analysis method with the simple principle is currently the most popular used method to predict shale gas well production (Lee and Sidle, 2010) and includes the Arps model (Arps, 1945), power law loss ratio rate decline model (Ilk et al., 2008), Duong model (Duong, 2010), stretched exponential production decline model (SEPD) (Valkó and Lee, 2010), logistic growth model (LGM) (Clark et al., 2011), Weibull growth model (Mishra, 2012), and BP neural network model (Tian and Ju, 2016). The production decline analysis method can predict future gas well production quickly and intuitively, but it can only analyze production data under conditions of constant or nearly constant bottom-hole flowing pressure (BHP) and requires continuous and stable production data; that is, it is only applicable if the production variation of the well has a definite decreasing law (Yu et al., 2018).

The analytical solution method establishes a corresponding mathematical model based on the physical model of shale gas horizontal well-staged fracturing, and obtains the analytical solution of reservoir pressure using mathematical methods such as the Laplace transformation, while predicting production by combining the historical fitting of actual production data. Researchers have proposed a linear dual-porosity model (Bello and Wattenbarger, 2010), a fiveregion flow model (Stalgorova and Mattar, 2012; Zhang et al., 2016), a trilinear-flow model (Brown et al., 2011; Ozkan et al., 2011), and a triple-porosity model (Al-Ahmadi and Wattenbarger, 2011; Tivayanonda et al., 2012). Although the aforementioned models develop their own governing equations based on various shale gas reservoir zoning schemes and relate gas flows in each region through boundary conditions in different regions, finding analytical solutions to partial differential equations (PDEs) when variable or complex boundary conditions are encountered is difficult.

The governing equations of gas flow for different flow mechanisms in multiple media areas of the reservoir were established using a numerical simulation method, and the numerical solutions of the equations were found using finite element, finite difference, and finite volume methods (FEM, FDM, and FVM). The majority of production predictions are based on established commercial numerical simulation software such as CMG (Wu et al., 2021; Xue et al., 2022), Eclipse (Yan et al., 2015; Kang et al., 2019), and UNCONG (Li et al., 2015), whereas others have constructed their own mathematical models and used COMSOL or MATLAB to derive numerical solutions for production prediction (Cao et al., 2016; Zheng et al., 2016; Wang et al., 2018; Micheal et al., 2023). The numerical simulation method has the advantage of being more relevant, having more rigorous mathematical and physical rationale, and providing a better fit. However, the model has numerous parameters that must be calibrated, and the accuracy of the parameter calibration is dependent on fitting single data sets, such as production or BHP, resulting in a strong multi-solution character of the calibration results and the absence of more multidimensional and sensitive indicators to constrain the model. Furthermore, the three aforementioned methods fail to accurately analyze the adsorbed/free gas ratio during shale gas well production because

they are primarily concerned with predicting gas well production. As a result, researchers have been searching for novel indicators and techniques to better predict the shale gas well production and analyze the adsorbed/free gas ratio.

Recent studies have shown significant multi-stage isotope fractionation features in the gas well production process (Gao et al., 2017: Niemann and Whiticar. 2017: Zhang et al., 2018: Zhao et al., 2022), shale gas field degassing (Chen et al., 2016; Han et al., 2017; Luo et al., 2019), and core saturation degassing (Tao et al., 2020; Li et al., 2020a; Wei et al., 2021). The fractionation at each stage is closely related to the gas-in-place (GIP) (Luo et al., 2019; Niu et al., 2020; Ma et al., 2020; Li et al., 2022a), gas production process (Gao et al., 2017; Ci et al., 2019), adsorbed/free gas ratio (Liu et al., 2016; Liu et al., 2019; Li et al., 2022b), and boundary conditions (Li et al., 2021, 2022c). This study introduces a novel concept based on isotope fractionation for forecasting shale gas well production and assessing the adsorbed/free gas ratio during shale gas production. However, existing studies have primarily focused on the observation and qualitative analysis of isotope fractionation phenomena in shale gas well production processes, and established isotope fractionation models are only applicable to core-scale gas transport processes. For example, based on Fick's second law, Zhang and Krooss (2001) developed an isotope fractionation model for diffusion processes but ignored the influence of adsorptiondesorption. Based on a one-dimensional (1D) continuous flow equation and the Langmuir isothermal adsorption theory, Xia and Tang (2012) developed a diffusion and adsorption/desorption coupled isotope fractionation model that can characterise the isotope fractionation caused by gas transport within a homogeneous pore structure. Li et al. (2021) constructed an isotope fractionation model applicable to the core degassing process that combined fractures, matrix pores, and kerogen structural pores. Nevertheless, current isotope fractionation models are primarily constructed based on one-dimensional (1D) radial flow or unidirectional flow, making it difficult to effectively characterise the complex isotope fractionation behaviour caused by the coupling of multi-scale transport mechanisms within complex gas transport regions during shale gas production. For example, reservoir-scale shale gas well production is frequently regarded as a complex superposition of multi-scale gas transport processes within the hydraulic fracture (HF), stimulated reservoir volume (SRV), and unstimulated reservoir volume (USRV) regions (Ozkan et al., 2011; Jiang et al., 2019; Wang et al., 2019).

In this study, we propose a multi-scale gas transport regions coupled model for carbon isotope fractionation of methane during shale gas production based on Darcy's law, the continuity equation, Fick's diffusion law, the Langmuir equation, and the isotopologues competing adsorption theory. Under varied BHP conditions, the model caters to multiple gas flow mechanisms (seepage, diffusion, and adsorption/desorption) within multi-scale gas transport regions (HF, SRV, and USRV regions) and attains an effective fit for the gas production rate, cumulative gas production, and $\delta^{13}C_1$ value under variable BHP conditions. We investigated the features and influencing factors of isotope fractionation during shale gas production using the proposed multi-scale gas transport regions coupled isotope fractionation model, quantitatively revealed the superposition effect and mechanism of isotope fractionation, established an approach to forecasting the shale gas well production, evaluated the adsorbed/free gas ratio during shale gas production, and performed a pilot application in the Jiaoshiba area of the Sichuan Basin, China, with positive assessment results, showing the tremendous potential of the proposed isotope fractionation model.

2. Model and simplification

After large-scale hydraulic fracturing operations, shale reservoirs may feature a hydraulic fracture network system with intricate geometry and a high-permeability region stimulated by fractures. As a result, a shale reservoir was divided into three gas transport regions (Fig. 1): hydraulic fracture (HF), stimulated reservoir volume (SRV), and unstimulated reservoir volume (USRV) region. The HF region is an apparent gas transport region composed of hydraulic fractures and the micro-fractures and macro-pores that surround hydraulic fractures. The SRV/USRV region is an apparent gas transport region composed of organic pores, inorganic pores, and micro-fractures. For ease of calculation, our model selects three HF regions as the basic simulation units (see Fig. 2).

The occurrence states and gas-transport mechanisms differ in each region. The gas inside the HF region is primarily free state and flows out as seepage, and the gas mass balance equation is frequently used to describe the gas transport in this region (Hu et al., 2022). Gas exists in both free and adsorbed states inside the SRV/USRV regions (Nie, 2023), and numerous gas transport mechanisms exist, including viscous flow, Knudsen diffusion, and surface diffusion (Bird et al., 2002; Ho and Webb, 2006). The specific transport method used by gas molecules is determined by the relationship between pore diameter and mean free path. We consider gas transport in the SRV and USRV regions as free gas diffusion (the synergistic effect of Knudsen diffusion and viscous flow) inside the pore space and desorption (surface diffusion) of adsorbed gas on the pore wall, thus a one-dimensional (1D) continuous flow equation is often used to describe the gas transport process (Cui et al., 2009). Under in-situ conditions, multi-scale coupled shale reservoirs require the consideration of gas flow between distinct gas transport regions, and traditional plate or column one-dimensional flow equations may not be appropriate. Therefore, based on previous work, we propose a threedimensional (3D) continuous flow equation (Appendix A shows the derivation process) to describe gas transport in the SRV/USRV regions. To summarise, the fundamental assumptions of this model are as follows: (1) The model incorporates three continuous flow regions: HF, SRV, and USRV, where free gas exists exclusively in the HF region, and both free gas and adsorbed gas are present in the SRV and USRV regions. (2) In the HF region, no isotope fractionation occurs, and ¹²CH₄ and ¹³CH₄ have identical diffusion coefficients. (3) In the SRV and USRV regions, the diffusion coefficient of ¹²CH₄ and ¹³CH₄ in matrix pore is represented as an apparent value, which effectively combines the viscous flow, Knudsen diffusion, and surface diffusion coefficients. Notably, the apparent diffusion coefficient of ¹²CH₄ exceeds that of ¹³CH₄. (4) The ¹²CH₄ and ¹³CH₄ in adsorbed gas follow the Langmuir isothermal adsorption equation and the isotopic competitive adsorption theory during adsorption/desorption processes. (5) The influence of multicomponent gases is not considered; shale gas consists of methane as a single-component gas. (6) The reservoir temperature is assumed to remain constant during production. (7) The effects of water on gas flow and isotope fractionation are not considered.

2.1. Governing equation

2.1.1. HF region

After the volumetric fracturing of the shale gas reservoir, a hydraulic fracture network system was formed, centred on each cluster of injection holes. The hydraulic fracturing network system is an essential channel for shale gas transportation, and the transportation capacity of the gas network is a critical factor influencing production capacity after fracturing. Using Ozkan's trilinear flow model, we treated the hydraulic fracture network system as an

equivalent high-permeability flow region (Ozkan et al., 2011). Taking into account the seepage effect of free gas in the hydraulic fracture, the PDEs (Appendix A shows the derivation process) for the transport of ¹²CH₄ and ¹³CH₄ molecules in the HF region are as follows:

$$\begin{cases} \phi_{F} \frac{\partial P_{F}}{\partial t} = K_{F} \nabla^{2} P_{F} \\ \phi_{F} \frac{\partial P_{F}^{*}}{\partial t} = K_{F} \nabla^{2} P_{F}^{*} \end{cases}$$
(1)

where $P_{\rm F}$ is the pressure of the $^{12}{\rm CH_4}$ in the HF region, Pa; $\phi_{\rm F}$ is the porosity of the HF region; and $K_{\rm F}$ is the apparent transport coefficient of the HF region, ${\rm m^2/s}$. The labelled * represents the physical quantity of $^{13}{\rm CH_4}$ molecules, while the unlabelled * represents the physical quantity of $^{12}{\rm CH_4}$ molecules.

2.1.2. SRV region

The multiple-fractured horizontal well (MFHW) was enclosed by a stimulated reservoir volume (SRV) region. This region is impacted by fracture communication and has a larger gas flow capacity than the unstimulated reservoir volume (USRV) region. Taking into account the diffusion of free gas and the adsorption/desorption of adsorbed gas in the matrix pores, the PDEs (Appendix A shows the derivation process) for the transport of ¹²CH₄ and ¹³CH₄ molecules in the SRV region are

$$\begin{cases} (C_{1_I}B_{2_I} - C_{2_I}B_{1_I}) \frac{\partial P_{\rm I}}{\partial t} = \nabla \cdot (B_{2_I}D_{\rm I}\nabla P_{\rm I} - B_{1_I}D_{\rm I}^*\nabla P_{\rm I}^*) \\ (C_{1_I}B_{2_I} - C_{2_I}B_{1_I}) \frac{\partial P_{\rm I}^*}{\partial t} = \nabla \cdot (C_{1_I}D_{\rm I}^*\nabla P_{\rm I}^* - C_{2_I}D_{\rm I}\nabla P_{\rm I}) \end{cases}$$
(2)

with

$$\begin{cases} B_{1_I} = -\frac{(1 - \phi_I)cKK^*P_I}{(1 + KP_I + K^*P_I^*)^2} \\ C_{1_I} = \phi_I + \frac{(1 - \phi_I)c(K + KK^*P_I^*)}{(1 + KP_I + K^*P_I^*)^2} \\ B_{2_I} = \phi_I + \frac{(1 - \phi_I)c(K^* + KK^*P_I)}{(1 + KP_I + K^*P_I^*)^2} \\ C_{2_I} = -\frac{(1 - \phi_I)cKK^*P_I^*}{(1 + KP_I + K^*P_I^*)^2} \end{cases}$$

$$(3)$$

where $P_{\rm I}$ is the pressure of $^{12}{\rm CH_4}$ in the SRV region, Pa; $\phi_{\rm I}$ is the effective porosity of the SRV region; K is the Langmuir constant, Pa $^{-1}$; c is the mass balance ratio ($c = \rho_{\rm rock} V_{\rm L} ZRT/V_{\rm m}$, Pa; $\rho_{\rm rock}$ is the apparent rock density, g/cm 3 ; $V_{\rm L}$ represents the utmost amount of gas that can be adsorbed per unit mass of rock, cm 3 /g; Z is gas compressibility factor; R is the ideal gas constant, 8.314 J mol $^{-1}$ K $^{-1}$; T is the reservoir temperature, K; $V_{\rm m}$ is the molar volume constant of the gas standard condition, 0.0224 m 3 /mol); and $D_{\rm I}$ is the diffusion coefficient in the SRV region, m 2 /s.

2.1.3. USRV region

The permeability of tight sedimentary rocks increases by 2–3 orders of magnitude after hydraulic fracturing compared with that before fracturing (Ge et al., 2018), and there is a positive relationship between permeability and diffusion coefficient. Therefore, the diffusion coefficient of the SRV region (D_1) in this model is two to three orders of magnitude greater than that of the USRV region (D_0). There were more micro-fractures in the SRV region than in the

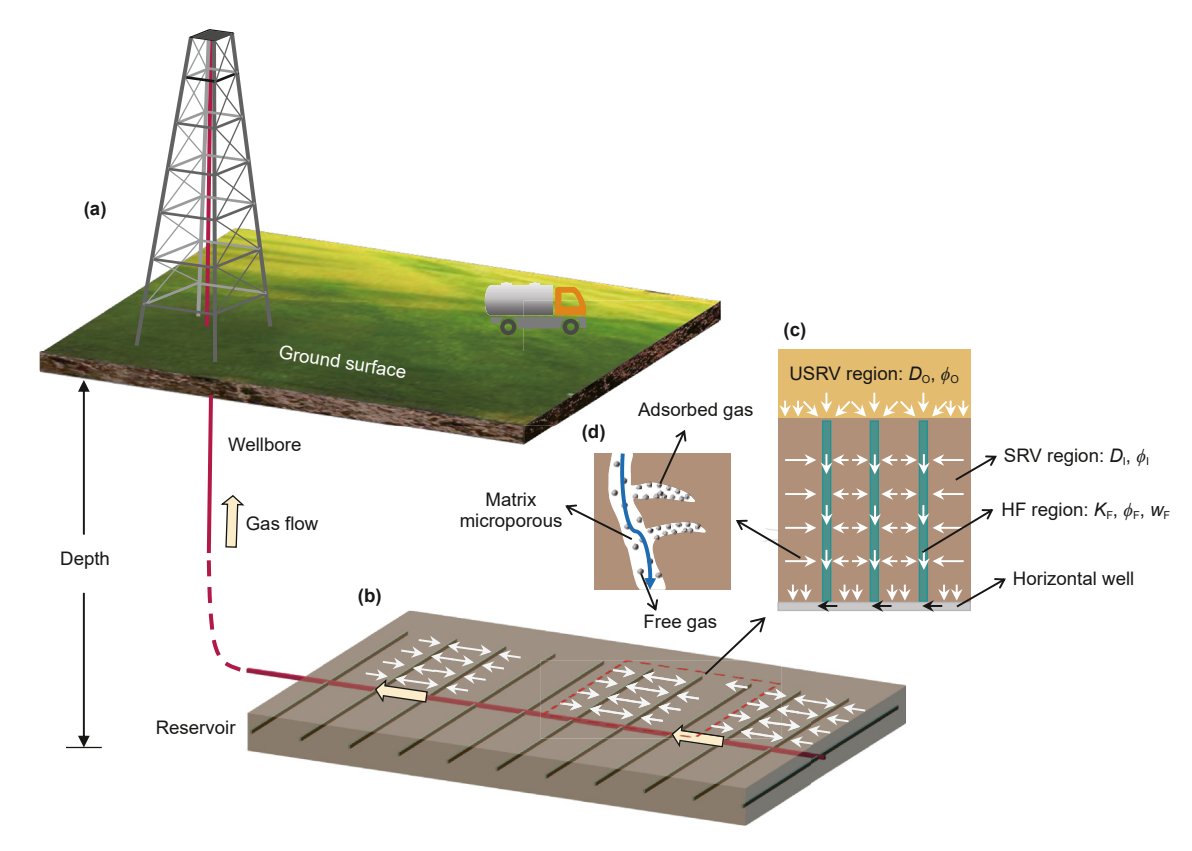


Fig. 1. Schematic diagram of multi-scale gas transport regions for a shale gas reservoir. The subscript F represents the parameters related to the HF region, the subscript I represents the parameters related to the SRV region (inner reservoir), and the subscript O represents the parameters related to the USRV region (outer reservoir).

USRV region as a consequence of stimulation by hydraulic fracturing; however, the increased volume of micro-fractures was small in comparison to the reservoir volume. Therefore, the porosity of the USRV region (ϕ_0) was slightly lower than that of the SRV region (ϕ_1). Although the reservoirs' petrophysical parameters differ, the mechanisms of internal gas transport are similar. As a result, the same equation was used for characterisation; however, the parameter values of the equation differed. Similarly, we considered free gas diffusion as well as the adsorption/desorption of adsorbed gas in the matrix pores. The PDEs for the transport of $^{12}\text{CH}_4$ and $^{13}\text{CH}_4$ molecules in the USRV region are

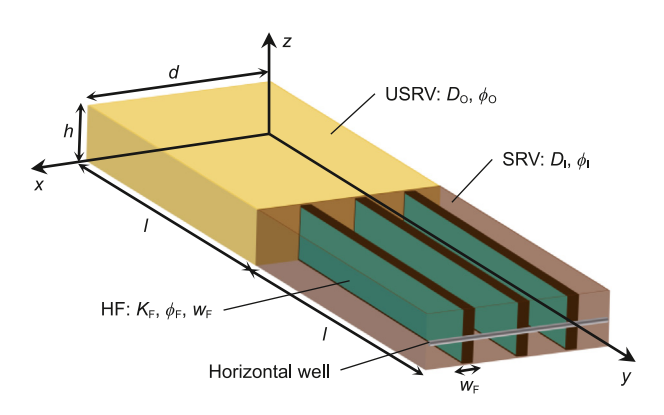


Fig. 2. Schematic diagram of the isotope fractionation theoretical model during shale gas production.

$$\begin{cases} (C_{1_0}B_{2_0} - C_{2_0}B_{1_0}) \frac{\partial P_0}{\partial t} = \nabla \cdot (B_{2_0}D_0\nabla P_0 - B_{1_0}D_0^*\nabla P_0^*) \\ (C_{1_0}B_{2_0} - C_{2_0}B_{1_0}) \frac{\partial P_0^*}{\partial t} = \nabla \cdot (C_{1_0}D_0^*\nabla P_0^* - C_{2_0}D_0\nabla P_0) \end{cases}$$

$$(4)$$

with

$$\begin{cases} B_{1-O} = -\frac{(1-\phi_{O})cKK^{*}P_{O}}{(1+KP_{O}+K^{*}P_{O}^{*})^{2}} \\ C_{1-O} = \phi_{O} + \frac{(1-\phi_{O})c(K+KK^{*}P_{O}^{*})}{(1+KP_{O}+K^{*}P_{O}^{*})^{2}} \\ B_{2-O} = \phi_{O} + \frac{(1-\phi_{O})c(K^{*}+KK^{*}P_{O})}{(1+KP_{O}+K^{*}P_{O}^{*})^{2}} \\ C_{2-O} = -\frac{(1-\phi_{O})cKK^{*}P_{O}^{*}}{(1+KP_{O}+K^{*}P_{O}^{*})^{2}} \end{cases}$$
(5)

2.2. Boundary conditions

2.2.1. Controlled boundary conditions

The partial pressures of ¹²CH₄ and ¹³CH₄ on the horizontal well column surface were equal to their respective ratios to the bottomhole flowing pressure (BHP).

$$P(t)|_{S_{\text{well}}} = P_{\text{wf}}(t) / \left(1 + n_{^{13}\text{CH}_4} / n_{^{12}\text{CH}_4}\right)$$
 (6)

$$P^{*}(t)|_{S_{\text{well}}} = P_{\text{wf}}(t) \cdot \left(n_{^{13}\text{CH}_{4}} / n_{^{12}\text{CH}_{4}}\right) / \left(1 + n_{^{13}\text{CH}_{4}} / n_{^{12}\text{CH}_{4}}\right)$$
 (7)

with

$$S_{\text{well}}: y = 2l - \sqrt{r_{\text{W}}^2 - (z + 0.5h)^2}, x \in (0, d), z \in (0.5h - r_{\text{W}}, 0.5h + r_{\text{W}})$$
(8)

$$n_{^{13}\text{CH}_4} / n_{^{12}\text{CH}_4} = (\delta_0 / 1000 + 1) \cdot R_{\text{st}}$$
 (9)

where $P_{\rm wf}$ is the BHP, MPa; $n_{^{13}{\rm CH_4}}/n_{^{12}{\rm CH_4}}$ is the initial molar ratio of $^{12}{\rm CH_4}$ to $^{13}{\rm CH_4}$; δ_0 is the initial carbon isotopic value; $R_{\rm st}$ is the carbon isotope atomic ratio of the PDB standard samples, 0.0112372; l is the half-length of the HF region, m; $r_{\rm w}$ is the radius of the horizontal well, m; d, 2l and h are the dimensions of the model in the x, y, and z directions, respectively, m.

2.2.2. Continuity boundary conditions

The instantaneous fluxes of 12 CH₄ or 13 CH₄ inflow and outflow at the interface between the SRV and HF regions were equal.

$$D_{l} \frac{\partial P_{l}}{\partial x} |_{S_{l-F}} = K_{F} \frac{\partial P_{F}}{\partial x} |_{S_{l-F}}$$
(10)

$$D_{l} \frac{\partial P_{l}^{*}}{\partial x} \Big|_{S_{l-F}} = K_{F} \frac{\partial P_{0}^{*}}{\partial x} \Big|_{S_{l-F}}$$

$$\tag{11}$$

The instantaneous pressures of $^{12}\text{CH}_4$ and $^{13}\text{CH}_4$ at the interface between the SRV and HF regions were equal.

$$P_{\rm I}|_{S_{\rm LF}} = P_{\rm F}|_{S_{\rm L-F}} \tag{12}$$

$$P_{\rm I}^*|_{S_{\rm I-E}} = P_{\rm F}^*|_{S_{\rm I-F}} \tag{13}$$

with

$$S_{I-F}: x = \left(\frac{1}{6}d \pm \frac{1}{2}w_F\right) \cup \left(\frac{1}{2}d \pm \frac{1}{2}w_F\right) \cup \left(\frac{5}{6}d \pm \frac{1}{2}w_F\right), y \in (l, 2l),$$

$$z \in (0, h)$$
(14)

where w_F is the width of the HF region, m.

The instantaneous fluxes of ¹²CH₄ or ¹³CH₄ at the interface between the USRV and HF regions were equal.

$$\begin{cases} \left. \frac{\partial P}{\partial x} \right|_{x=0,y\in(0,2l),z\in(0,h)} = \frac{\partial P^*}{\partial x} \left| \right._{x=d,y\in(0,2l),z\in(0,h)} = 0 \\ \left. \left. \frac{\partial P}{\partial y} \right|_{y=0,x\in(0,d),z\in(0,h)} = \frac{\partial P^*}{\partial y} \left| \right._{y=2l,x\in(0,d),z\in(0,0.5h-r_w)\cup(0.5h+r_w,h)} = 0 \\ \left. \frac{\partial P}{\partial z} \right|_{z=0,y\in(0,2l),x\in(0,d)} = \frac{\partial P^*}{\partial z} \left| \right._{z=h,y\in(0,2l),x\in(0,d)} = 0 \end{cases}$$

$$D_{O} \frac{\partial P_{O}}{\partial \nu}|_{s_{O-F}} = K_{F} \frac{\partial P_{F}}{\partial \nu}|_{s_{O-F}}$$
(15)

$$D_{0} \frac{\partial P_{0}^{*}}{\partial y} |_{s_{0-F}} = K_{F} \frac{\partial P_{F}^{*}}{\partial y} |_{s_{0-F}}$$

$$\tag{16}$$

The instantaneous pressures of ¹²CH₄ and ¹³CH₄ at the interface between the SRV and USRV regions are equal.

$$P_{\rm O}|_{\rm S_{\rm O-F}} = P_{\rm F}|_{\rm S_{\rm O-F}} \tag{17}$$

$$P_{\rm O}^*|_{S_{\rm O-F}} = P_{\rm F}^*|_{S_{\rm O-F}} \tag{18}$$

with

$$S_{0-F}: y = l, x \in \left(\frac{1}{6}d - \frac{1}{2}w_F, \frac{1}{6}d + \frac{1}{2}w_F\right) \cup \left(\frac{1}{2}d - \frac{1}{2}w_F, \frac{1}{2}d + \frac{1}{2}w_F\right)$$

$$\cup \left(\frac{5}{6}d - \frac{1}{2}w_F, \frac{5}{6}d + \frac{1}{2}w_F\right), z \in (0, h)$$
(19)

The instantaneous fluxes of $^{12}CH_4$ or $^{13}CH_4$ at the interface between the SRV and USRV regions are equal.

$$D_{l} \frac{\partial P_{l}}{\partial y} |_{s_{l-0}} = D_{0} \frac{\partial P_{0}}{\partial y} |_{s_{l-0}}$$
(20)

$$D_{l} \frac{\partial P_{l}^{*}}{\partial \nu} |_{s_{l-0}} = D_{0} \frac{\partial P_{0}^{*}}{\partial \nu} |_{s_{l-0}}$$

$$\tag{21}$$

The instantaneous pressures of ¹²CH₄ and ¹³CH₄ at the interface between the SRV and USRV regions are equal.

$$P_{1}|_{s_{1-0}} = P_{0}|_{s_{1-0}} \tag{22}$$

$$P_{\rm I}^*|_{s_{\rm I-O}} = P_{\rm O}^*|_{s_{\rm I-O}} \tag{23}$$

with

$$S_{I-O}: y = l, x \in \left(0, \frac{1}{6}d - \frac{1}{2}w_F\right) \cup \left(\frac{1}{6}d + \frac{1}{2}w_F, \frac{1}{2}d - \frac{1}{2}w_F\right) \\ \cup \left(\frac{1}{2}d + \frac{1}{2}w_F, \frac{5}{6}d - \frac{1}{2}w_F\right) \cup \left(\frac{5}{6}d + \frac{1}{2}w_F, d\right), z \in (0, h)$$

$$(24)$$

2.3. Insulation boundary conditions

There are no inflow and outflow fluxes at the outer boundaries of the model.

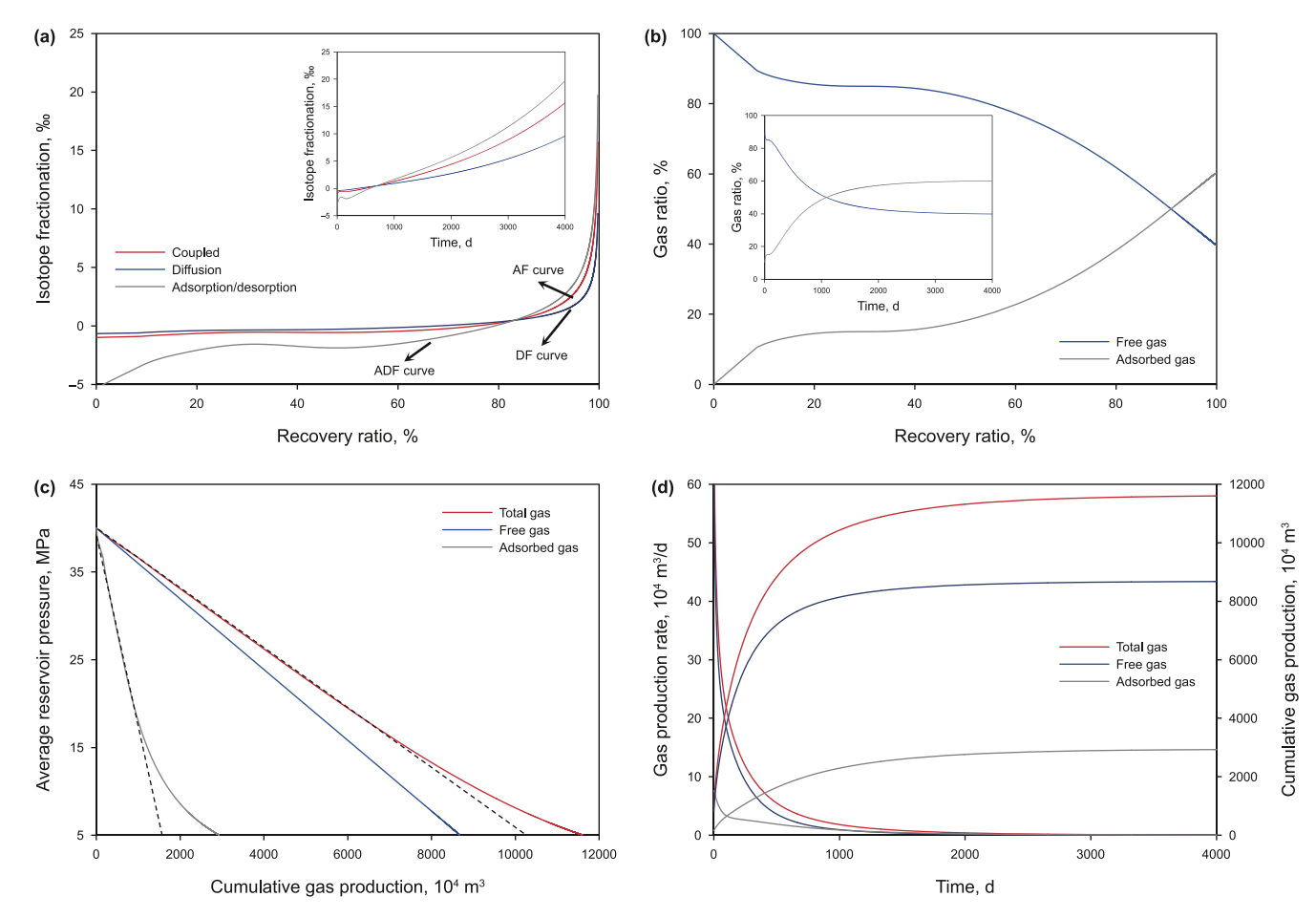


Fig. 3. Effect of diffusion and adsorption/desorption on gas production rate and isotope fractionation. Parameters: $P_0 = 40$ MPa; $P_{wf} = 5$ MPa; $P_{wf} = 2.6$ g/cm³; $\phi_l = 0.05$; T = 416 K; $D_l^*/D_l = 0.999$; $D_l = 10^{-7}$ m²/s; $\delta_0 = -30\%$; $P_L(1/K) = 5$ MPa; $V_L = 4$ cm³/g. Simulation model dimension: 150 m × 73 m × 25 m. Reservoir dimension: 150 m × 1022 m × 25 m. The calculation formulas for isotope fractionation, gas production rate, gas ratio, and recovery ratio are shown in Appendix B.

2.4. Initial conditions

Initially, the partial pressures of ¹²CH₄ and ¹³CH₄ in each region were equal to the partial pressure of the initial reservoir.

$$P_{\rm F}(t=0) = P_{\rm I}(t=0) = P_{\rm O}(t=0) = P_{\rm O} / \left(1 + n_{^{13}{\rm CH}_4} / n_{^{12}{\rm CH}_4}\right) \tag{26}$$

$$P_{F}^{*}(t=0) = P_{I}^{*}(t=0) = P_{O}^{*}(t=0)$$

$$= P_{O} \cdot \left(n_{^{13}CH_{4}} / n_{^{12}CH_{4}}\right) / \left(1 + n_{^{13}CH_{4}} / n_{^{12}CH_{4}}\right)$$
(27)

where P_0 is the initial reservoir pressure, Pa.

3. Parameters, results, and discussion

3.1. Effect of diffusion and adsorption/desorption

Methane can become adsorbed on the surfaces of kerogen and clay minerals as well as stored as free gas in the pores of argillaceous source rocks. Adsorbed gas represents 20%–85% of the total gas at these storage locations (Curtis, 2002). Free and adsorbed gases are critical components in determining the shale gas reservoir gas-in-place (GIP), and the adsorbed/free gas ratio determines the lifespan of shale gas wells to some extent. As a result, the effects

of diffusion and adsorption/desorption on gas production rate and isotope fractionation must be investigated.

In this section, we ignore the influence of the USRV and HF regions to investigate the effects of diffusion and adsorption/ desorption on gas flow and isotope fractionation in the SRV region at a constant BHP. The diffusion fractionation (DF) curve with free gas contribution, the adsorption/desorption fractionation (ADF) curve with adsorbed gas contribution, and the apparent fractionation (APP) curve with free gas and adsorbed gas coupled are shown in Fig. 3(a). The isotope fractionation curve is calculated by subtracting the initial isotopic value from the instantaneous isotopic value of the produced gas (δ_{ins} – δ_0). The three curves exhibited a monotonically increasing trend as production progressed. The produced gas was dominated by free gas during early and middle production, and the APP curve is close to the DF curve. As the reservoir pressure decreased, the adsorbed gas began to desorb significantly, becoming the primary source of the produced gas (Fig. 3(b)). As a result, the APP curve begins to approach the ADF fractionation curve during late production. There is a special phenomenon where there is a reversal point between the ADF curve and the APP curve during early production. This is because light isotope molecules are preferentially desorbed (Xia and Tang, 2012). In addition to influencing isotope fractionation, diffusion and adsorption/desorption have an impact on the cumulative gas production and gas production rate. In the early to middle production periods, the cumulative gas production increased linearly with decreasing average reservoir pressure (Fig. 3(c)), indicating that

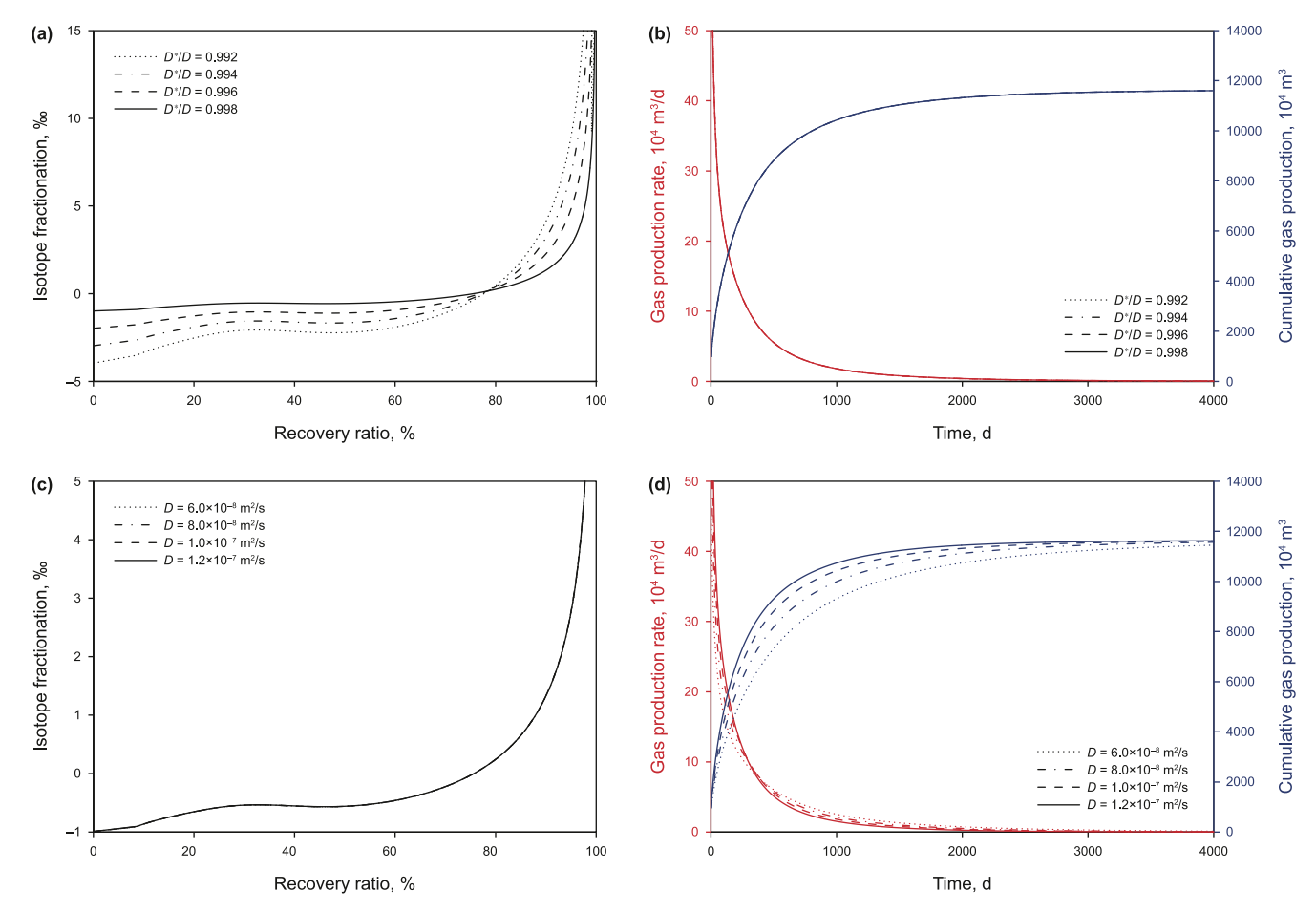


Fig. 4. Effect of diffusion on the gas production rate and isotope fractionation. Parameters: The fundamental parameters are identified as those in Fig. 3.

free gas is the primary contributor to the produced gas. During late production, a considerable proportion of adsorbed gas is desorbed, resulting in a nonlinear increase in cumulative gas production as the average reservoir pressure decreases. This phenomenon was comparable to the laboratory results obtained by Hu et al. (2021). After approximately 1000 days, the gas production rapidly decreased into a lengthy stage of low-stability production (Fig. 3(d)), and the arrival time of this low-stability production stage was closely related to the initial reservoir pressure, petrophysical parameters, and BHP.

3.1.1. Effect of diffusion

(1) D*/D

 D^*/D represents the relative diffusion capacity of the $^{12}\text{CH}_4$ and $^{13}\text{CH}_4$ molecules. According to the law of kinetic energy, the rate of molecular transportation at the same temperature is inversely proportional to the square root of its mass, so the diffusion coefficient of $^{13}\text{CH}_4$ molecule is smaller than that of $^{12}\text{CH}_4$ molecule $(D^* < D)$, i.e., D^*/D is usually less than 1. The difference in diffusion coefficients between $^{12}\text{CH}_4$ and $^{13}\text{CH}_4$ molecule is an intrinsic factor in isotope kinetic fractionation. When the gas transport channel is much larger than the molecular diameter, the difference in diffusion coefficients between $^{12}\text{CH}_4$ and $^{13}\text{CH}_4$ molecule is smaller, and when the gas transport channel is smaller, the difference in diffusion coefficients between $^{12}\text{CH}_4$ and $^{13}\text{CH}_4$ molecule will be more obvious. For a specific molecule and temperature-pressure

conditions, the average pore size determines D^*/D during gas transport in rocks.

The effect of D^*/D on isotope fractionation is evident during gas transport. The more D^*/D is below 1, the slower the diffusion of ¹³CH₄ molecules relative to ¹²CH₄ molecules, the smaller the proportion of ¹³CH₄ molecules in the produced gas during early and middle production, and the greater the proportion of ¹³CH₄ molecules in the produced gas during late production. Therefore, the more D^*/D is less than 1, the more negative the $\delta_{\rm ins}$ value during early/middle production, and the more positive it is during late production, that is, the greater the isotope fractionation amplitude (Fig. 4(a)). It could be claimed that the more obvious the isotope fractionation, the smaller the average pore size of the rock is since the smaller D^*/D symbolizes the smaller average pore size of the rock. This conclusion also confirms that isotope fractionation is more likely to be found in the production of unconventional dense sedimentary rock reservoirs such as shale, coal, and dense sandstone compared to conventional sandstone reservoirs. Variation of D^*/D has little effect on the gas production rate and cumulative gas production (Fig. 4(b)), because small changes in D^*/D affect the relative diffusion capacity of ¹²CH₄ and ¹³CH₄ molecules in the pore space, but have little effect on the total diffusion capacity of CH₄ $(D + D^*).$

(2) D

D is the diffusion coefficient of $^{12}\mathrm{CH_4}$ molecules in the matrix pores (in this model, D is the apparent value combining the viscous

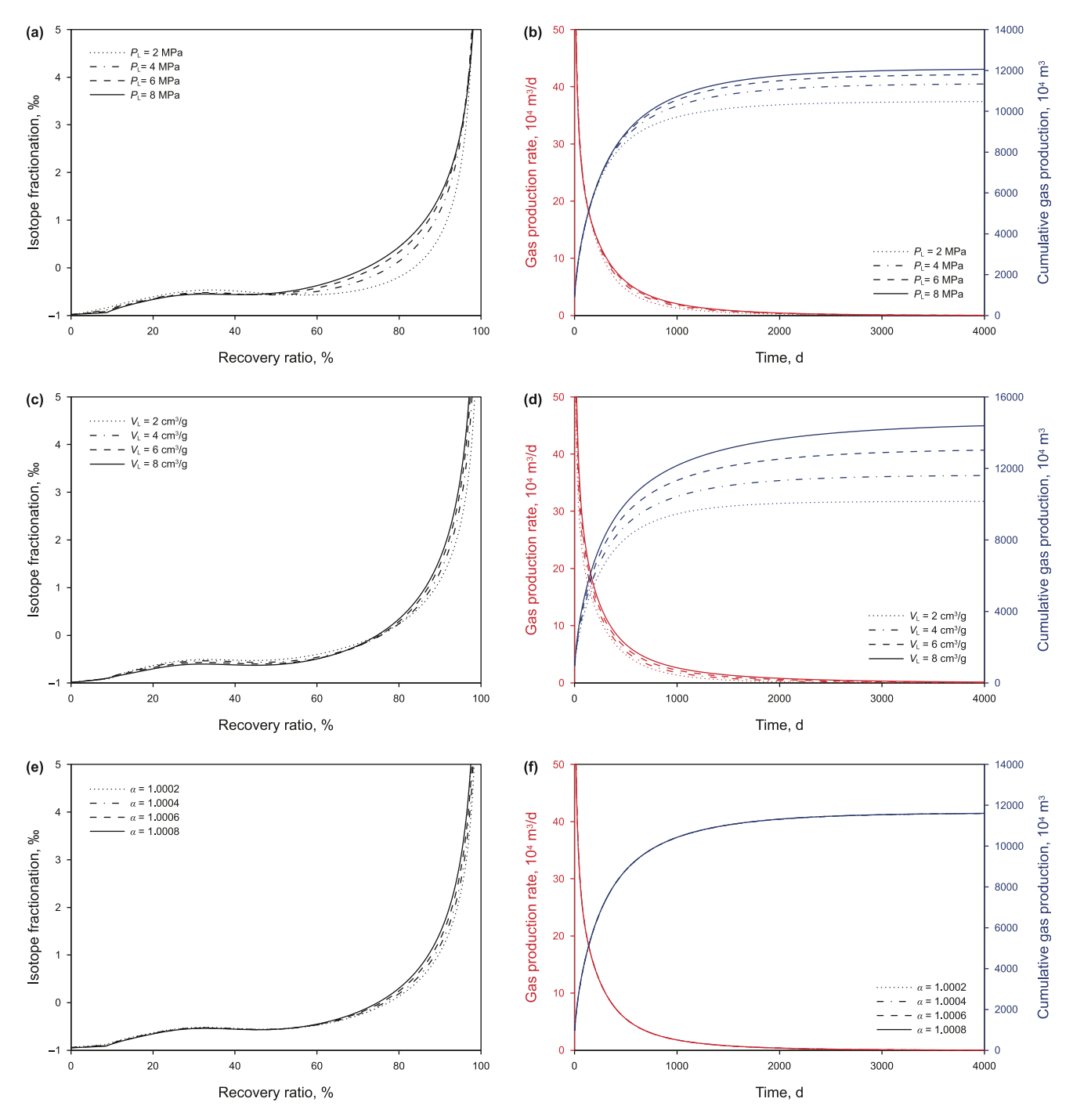


Fig. 5. Effect of adsorption/desorption on gas production rate and isotope fractionation. Parameters: The fundamental parameters are identified as those in Fig. 3.

flow diffusion coefficient and Knudsen diffusion coefficient). D is a critical parameter that measures gas diffusion capacity; the higher D, the faster methane molecules move. However, the fluctuation in D had essentially no effect on isotope fractionation (Fig. 4(c)). Because increasing D increases D^* in the same proportion for a given D^*/D , the variation in D at a given recovery ratio has essentially little influence on the ratio of $^{12}\text{CH}_4$ and $^{13}\text{CH}_4$ molecules in the produced gas. The changes in D played a significant role in production, with a higher gas production rate and greater D during early production (0–400 days) and progressively opposite results

beyond 400 days (Fig. 4(d)). This is because, for a given reservoir energy, a faster initial production rate causes the reservoir energy to decline quickly, resulting in insufficient production capacity later on (Li, 2020b).

For D and D^*/D , two parameters related to the diffusion effect, variation in D has a significant impact on the gas production rate but almost no effect on isotope fractionation, whereas variation in D^*/D has a considerable impact on isotope fractionation but almost no effect on gas production rate.

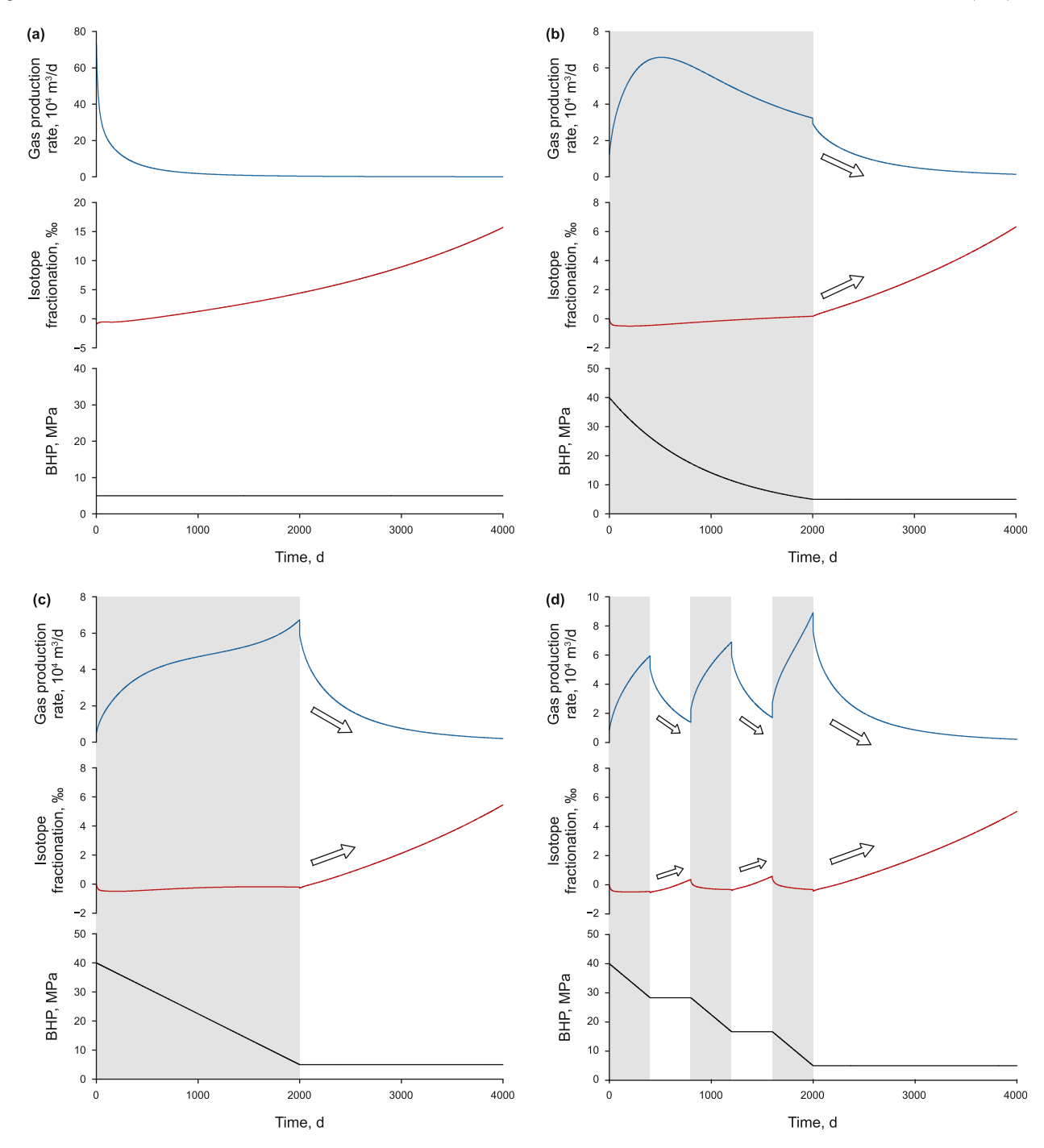


Fig. 6. Effect of different BHP on isotope fractionation and gas production rate. **(a)** $P_{\rm wf} = 5$ MPa; **(b)** 0-2000 days: $P_{\rm wf} = 40 \times \exp(-0.0010397t)$ MPa, 2000-4000 days: $P_{\rm wf} = 5$ MPa; **(c)** 0-2000 days: $P_{\rm wf} = -0.0175t + 40$ MPa, 2000-4000 days: $P_{\rm wf} = 5$ MPa; **(d)** 0-400 days: $P_{\rm wf} = -0.029t + 40$ MPa, 400-800 days: $P_{\rm wf} = 28.33$ MPa,800-1200 days: $P_{\rm wf} = -0.029 \times (t-400) + 40$ MPa, 1200-1600 days: $P_{\rm wf} = 16.667$ MPa, 1600-2000 days: $-0.029 \times (t-800) + 40$ MPa, 1200-4000 days: $P_{\rm wf} = 5$ MPa. The model's fundamental parameters are identical to those in Fig. 3.

3.1.2. Effect of adsorption/desorption

(1) $P_{L}(1/K)$

 $P_{\rm L}$ is the Langmuir pressure, which is inverse of the Langmuir constant (K) ($P_{\rm L}=1/K$). $P_{\rm L}$ describes the ability of a pore wall to adsorb gas molecules. The lower the $P_{\rm L}$, the greater the adsorption capacity of the rock and the easier it is for methane molecules to be adsorbed on the pore surface. The impact of $P_{\rm L}$ variation on isotope

fractionation was evident. During early production, the proportion of adsorbed gas to produced gas is low, and $P_{\rm L}$ variations have essentially no effect on the isotope fractionation curve. During middle production, the smaller $P_{\rm L}$, the more $^{13}{\rm CH_4}$ molecules are adsorbed by the rock, the fewer $^{13}{\rm CH_4}$ molecules are produced, and the more negative the $\delta_{\rm ins}$. During the late production, the adsorbed $^{13}{\rm CH_4}$ molecules in the early and middle production stages begin to be desorbed in significant quantities; the smaller the $P_{\rm L}$, the greater the proportion of desorbed $^{13}{\rm CH_4}$ molecules in the produced gas

and the more positive the δ_{ins} . This indicates that as the P_L decreases, the fractionation amplitude of the isotope curve increases (Fig. 5(a)). The role of P_L variation in production is also obvious: during the early production, when the produced gas has a low ratio of adsorbed gas, P_L variation has minimal impact on the production curve. During the middle/late production stages, as the proportion of adsorbed gas in the produced gas increases, the smaller the P_L , the higher the rock adsorption capacity for methane molecules, resulting in decreased cumulative gas production and gas production rate (Fig. 5(b)). This agrees with the outcomes of the numerical simulations by Zhao et al. (2020).

 $(2)V_{\rm L}$

 $V_{\rm L}$ is Langmuir volume, representing the largest quantity of gas that can be adsorbed per unit mass of rock. Under certain other parameters, the greater the V_L , the more the amount of adsorbed gas in the rock. V_L had a comparable effect on the isotope fractionation curve as P_{L} . During early production, the produced gas contained a relatively small proportion of adsorbed gas, and variations in V_L had little effect on the isotope fractionation curve. During middle production, ¹²CH₄ molecules are preferentially desorbed, and the larger the $V_{\rm L}$, the more $^{12}{\rm CH_4}$ molecules are produced and the more negative the δ_{ins} . During the late production, a substantial quantity of $^{13}\text{CH}_4$ molecules begins to desorb, and the larger the V_L , the more 13 CH₄ molecules are produced and the more positive the δ_{ins} . This implies that the fractionation amplitude of the isotope curve increases with increasing $V_{\rm I}$ (Fig. 5(c)). The influence of $V_{\rm L}$ variation on production is more intuitive, with a larger V_L producing more gas, resulting in a higher gas production rate and cumulative gas production (Fig. 5(d)).

 $(3) \alpha$

 α is the fractionation factor between the adsorbate and gas phase (Xia and Tang, 2012):

$$\alpha = (\theta^* / \theta) / (P^* / P) \tag{28}$$

where θ and θ * are the fractional coverage of adsorbed gas for $^{12}\text{CH}_4$ and $^{13}\text{CH}_4$, respectively. The relationship between coverage and pore internal pressure is

$$\begin{cases} \theta = \frac{KP}{1 + KP + K^*P^*} \\ \theta^* = \frac{K^*P^*}{1 + KP + K^*P^*} \end{cases}$$
 (29)

where K and K^* are the Langmuir constants of $^{12}\text{CH}_4$ and $^{13}\text{CH}_4$, respectively. By combining Eqs. (28) and (29), we obtain the relationship between α , K, and K^* as

$$\alpha = K^*/K \tag{30}$$

The difference in the adsorption strength of $^{12}\text{CH}_4$ and $^{13}\text{CH}_4$ molecules by the rock wall is reflected by α . The variation of α also has an effect on isotope fractionation. During the early to middle production period, the ratio of adsorbed gas in the produced gas is minimal, and the variation of α has almost no effect on the isotope fractionation curve. During the middle and late production, the ratio of adsorbed gas in the produced gas gradually increases, and the larger the α , the more obvious the difference in the adsorption strength of $^{12}\text{CH}_4$ and $^{13}\text{CH}_4$ molecules by the rock wall, and the greater the fractionation amplitude of the isotope fractionation curve (Fig. 5(e)). Similar to D^*/D , the variation of α has essentially

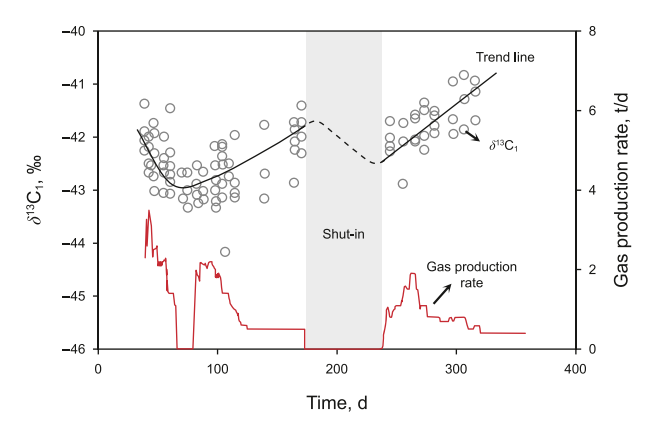


Fig. 7. Characteristic of gas production rate and methane carbon isotope changes in shale gas well HG101-X2 (Data is sourced from Ci et al. (2019)).

no effect on the gas production rate and the cumulative gas production (Fig. 5(f)).

 D^*/D and D are related to diffusion, and P_L , V_L , and α are related to adsorption/desorption; the five parameters affect both isotope fractionation and gas production rate of shale gas. The significance of their effects on isotope fractionation followed the order D^*/D , P_L , V_L , α , and D.

3.2. Effect of bottom-hole flowing pressure (BHP)

Various shale gas well production regimes result in distinct modes of declining BHP. and the BHP is closely related to gas production rate and isotope fractionation. The isotope fractionation curve exhibited a monotonically increasing trend relative to the monotonically decreasing gas production rate when produced at a constant BHP (Fig. 6(a)). Changing the BHP to decline exponentially or linearly to 5 MPa for the first 2000 days and then to a constant 5 MPa for the next 2000 days results in a mutation point in both the gas production rate curve and isotope fractionation curve at the junction of the different production regimes (Fig. 6(b) and (c)). This characteristic is particularly apparent in Fig. 6(d), which shows a multi-stage decline. The fractionation amplitude of the isotope fractionation curve is relatively small during the linear decline stage of BHP before the mutation point (grey area in Fig. 6). When entering the constant BHP production stage (white area in Fig. 6), the fractionation amplitude of the isotope fractionation curve increases, and the gas production rate enters a rapid decline stage. This phenomenon was also observed in the data from a previously measured production well (Fig. 7). Before the shut-in, the $\delta^{13}C_1$ first decreased and then increased. During the shut-in period, when the gas production rate was 0 (the grey area in Fig. 7), the $\delta^{13}C_1$ began to decline, but after the shut-in, the $\delta^{13}C_1$ started to increase again. It is consistent with the results obtained from numerical simulations.

We found an interesting phenomenon that the gas production rate curve and the isotope fractionation curve exhibit opposite trends during the constant BHP production stage, as indicated by the arrows in Fig. 6. Furthermore, the greater the fractionation amplitude of the isotope fractionation curve, the lower the gas production rate and the closer the gas well is to depletion. Ci et al. (2019) identified this phenomenon in 2019 using carbon isotope logging to determine whether a candidate well had retained reserves for secondary fracturing. They suggested that if the $\delta^{13}C_1$ of the produced gas becomes significantly positive and the fractionation amplitude is considerable, it indicates that free gas and the majority of the adsorbed gas have been produced, resulting in pressure depletion. This implies that the gas released within the

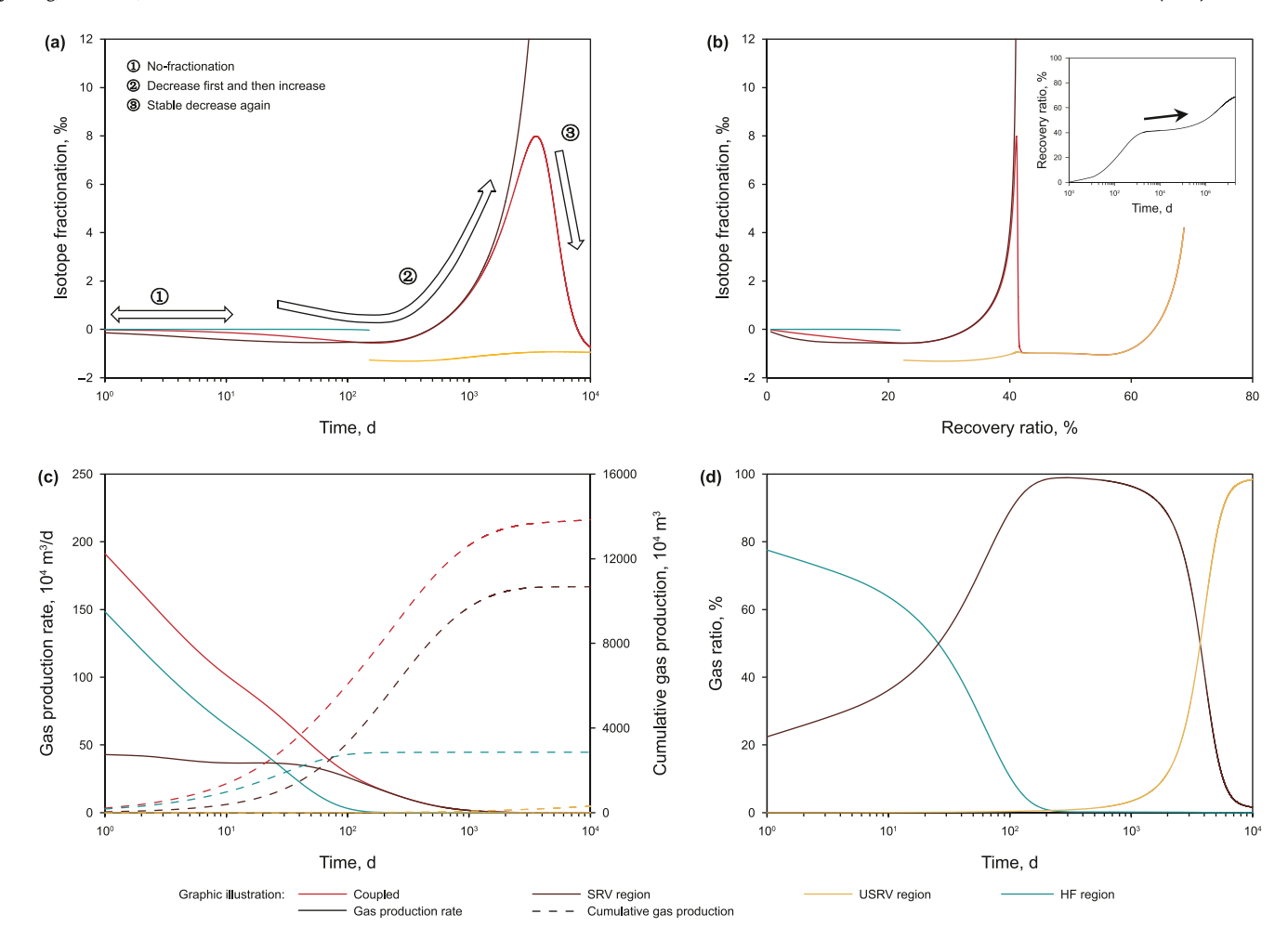


Fig. 8. Characteristics of gas production rate and isotope fractionation under multi-scale gas transport regions. Parameters: $P_0 = 40$ MPa; $P_{wf} = 5$ MPa; $\rho_{rock} = 2.6$ g/cm³; T = 416 K; $\delta_0 = -30\%$; $P_L(1/K) = 5$ MPa; $V_L = 4$ cm³/g; $w_F = 2$ m; $r_w = 0.1$ m; $\phi_I = 0.05$; $\phi_O = 0.04$; $\phi_F = 0.2$; $K_F = 0.005$ m²/s; $D_I = 1 \times 10^{-7}$ cm²/s; $D_O = 1 \times 10^{-9}$ cm²/s; $D_I * / D_I = 0.999$; $D_O * / D_O = 0.998$. Simulation model dimension: 300 m × 73 m × 25 m. Reservoir dimension: 600 m × 1022 m × 25 m.

initial fracturing release range was exhausted and could be diverted to new layers for fracturing. When the isotope fractionation amplitude of the produced gas is relatively small, it suggests that the fracture closed prematurely and that a large volume of undischarged gas remains within the release range of the fracture, which can be modified in the original fracture. Ci et al. (2019) discovered the relationship between the isotope fractionation and gas production rate and proposed a new application of the isotope tool. However, the shortcoming of this method is that differences in the diffusion-adsorption/desorption characteristics of different reservoirs can affect the magnitude of isotope fractionation, and it is difficult to provide a standard to determine whether the fractionation characteristic is obvious.

By identifying the $\delta^{13}C_1$ reversal point in the field-monitored isotopic data, Gao et al. (2017) determined the total reserves of a shale gas well in Barnett. They applied isotope techniques to predict production early, inspiring academics to conduct research on isotope fractionation and production prediction. However, their method is applicable to circumstances where the gas production rate of shale gas wells declines continuously and steadily (similar to Fig. 6(a)). When there are multi-stage fluctuations in production regimes, as illustrated in Fig. 6(d), the $\delta^{13}C_1$ data monitored in the field may exhibit multiple $\delta^{13}C_1$ reversal points, making it difficult to identify a truly controlled production reversal point to estimate the reserves of a shale gas well.

Different BHP have a substantial effect on isotope fractionation and gas production rate during shale gas production, providing theoretical guidance for determining which production regimes can assure long-term stability production and maximize the production benefits of gas wells.

3.3. Effect of multi-scale gas transport regions

3.3.1. Characteristics of gas flow and isotope fractionation

In Section 3.1, we discussed the gas production rate and isotope fractionation characteristics when gas flows only within the SRV region, and found that the $\delta_{\rm ins}$ value monotonically increases with production time (Fig. 3(a)). However, field monitoring in gas fields demonstrates that the $\delta^{\rm 13}C_1$ value shows significant multi-stage isotope fractionation as shale gas production progresses. This is because multi-scale gas transport regions exist in shale reservoirs under in situ geological conditions. Therefore, we considered gas flow with multi-mechanisms (seepage, diffusion, and adsorption or desorption) under the coupling of multi-scale gas transport regions (HF, SRV, and USRV) to analyze the isotope fractionation and gas production rate characteristics during shale gas well production.

Compared to the isotope fractionation curve for a single gas transport region (Fig. 3(a)), the superposition of multi-mechanism in multi-scale gas transport regions results in three significant alterations to the isotope fractionation curve: (1) a brief "no-

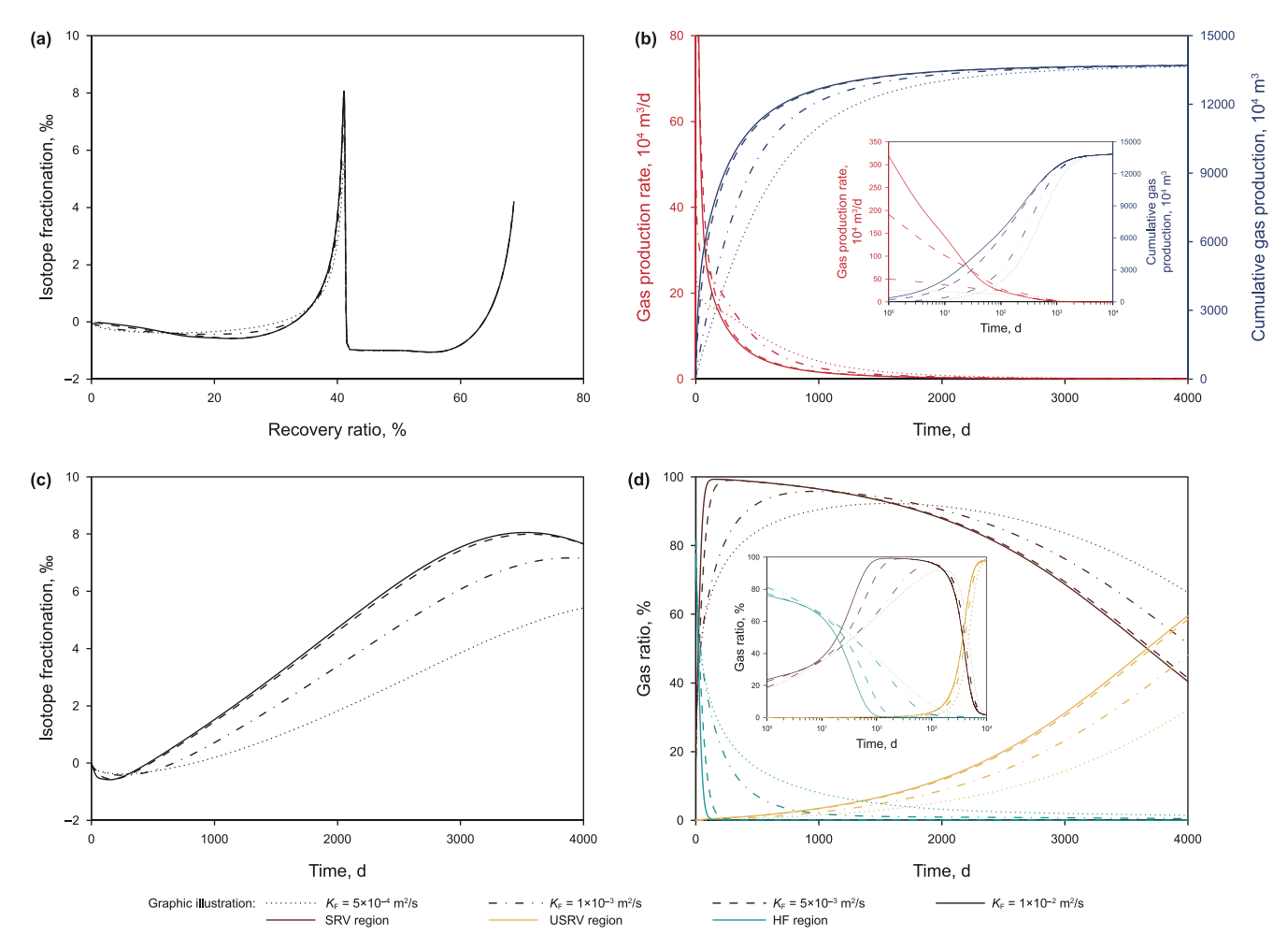


Fig. 9. Effect of K_F on isotope fractionation and gas production rate. The basic parameters are the same as in Fig. 8.

fractionation" feature during early production; (2) a "decrease first and then increase" feature during middle production; and (3) a "stable decrease again" feature during late production (Fig. 8(a) and (b)). Because the scale of the hydraulic fractures, micro-fractures, and macro-pores in the HF region is much larger than the methane molecular diameter, the difference in gas flow capacity between ¹²CH₄ and ¹³CH₄ molecules is insignificant in the HF region; thus, dynamic fractionation does not occur. During early production, HF region gas comprised a significant portion of the produced gas (Fig. 8(d)), resulting in a brief period of "no-fractionation" phenomenon on the coupled isotope fractionation curve. As the contribution of SRV region gas progressively increases during middle production, the coupled isotope fractionation curve approaches that of the SRV region fractionation curve, and the phenomenon of "decrease first and then increase" manifests. During late production, the SRV region gas has been produced in large quantities, the proportion of USRV region gas with more negative $\delta_{\rm ins}$ values gradually increases in the produced gas (Fig. 8(d)), and the coupled isotope fractionation curve approaches that of the USRV region fractionation curve with a "stable decrease again" phenomenon. The exploitation time required to improve the recovery ratio increases exponentially when the recovery ratio exceeds 0.4, as shown in the small graph in Fig. 8(b), indicating that it is difficult to utilize the low-permeability unfractured USRV region during shale gas development.

The characteristics of the coupled isotope fractionation curves that do not fractionate during early production can be utilized to assess the efficacy of fracturing. The fracturing effect of shale reservoirs is better, and the duration of HF region gas as the main contributor is longer, and the longer the isotope fractionation curve does not fractionate. When a gas well enters a long-term stable low-production stage during the late production, the characteristics of the "stable decrease again" of the isotope fractionation curve can be applied to assess the production state of the gas well and to evaluate the remaining reserves, providing theoretical support for subsequent construction operations such as shut-in on well or secondary fracturing.

3.3.2. Effect of HF region related parameters

 $(1) K_{\rm F}$

Cui et al. (2009) introduced the apparent transport coefficient to describe gas transport in dense reservoir rocks. Drawing on this concept, we introduced the apparent transport coefficient of the HF region (K_F) as the quotient obtained by dividing the permeability of the HF region (k_F) by the product of the porosity of the HF region (ϕ_F), gas viscosity (μ_g) and compression factor of HF region (C_F), i.e., $K_F = k_F/(\phi_F \times \mu_g \times C_F)$. The apparent transport coefficient (K_F) is proportional to the hydraulic fracture permeability (k_F) for a given ϕ_F , μ_g , and C_F and reflects the capacity of the HF region to transport gas. The larger the K_F , the faster the HF region gas is produced, and the faster the SRV region gas is replenished. The isotope fractionation curve with recovery ratio in the abscissa also reveals a more

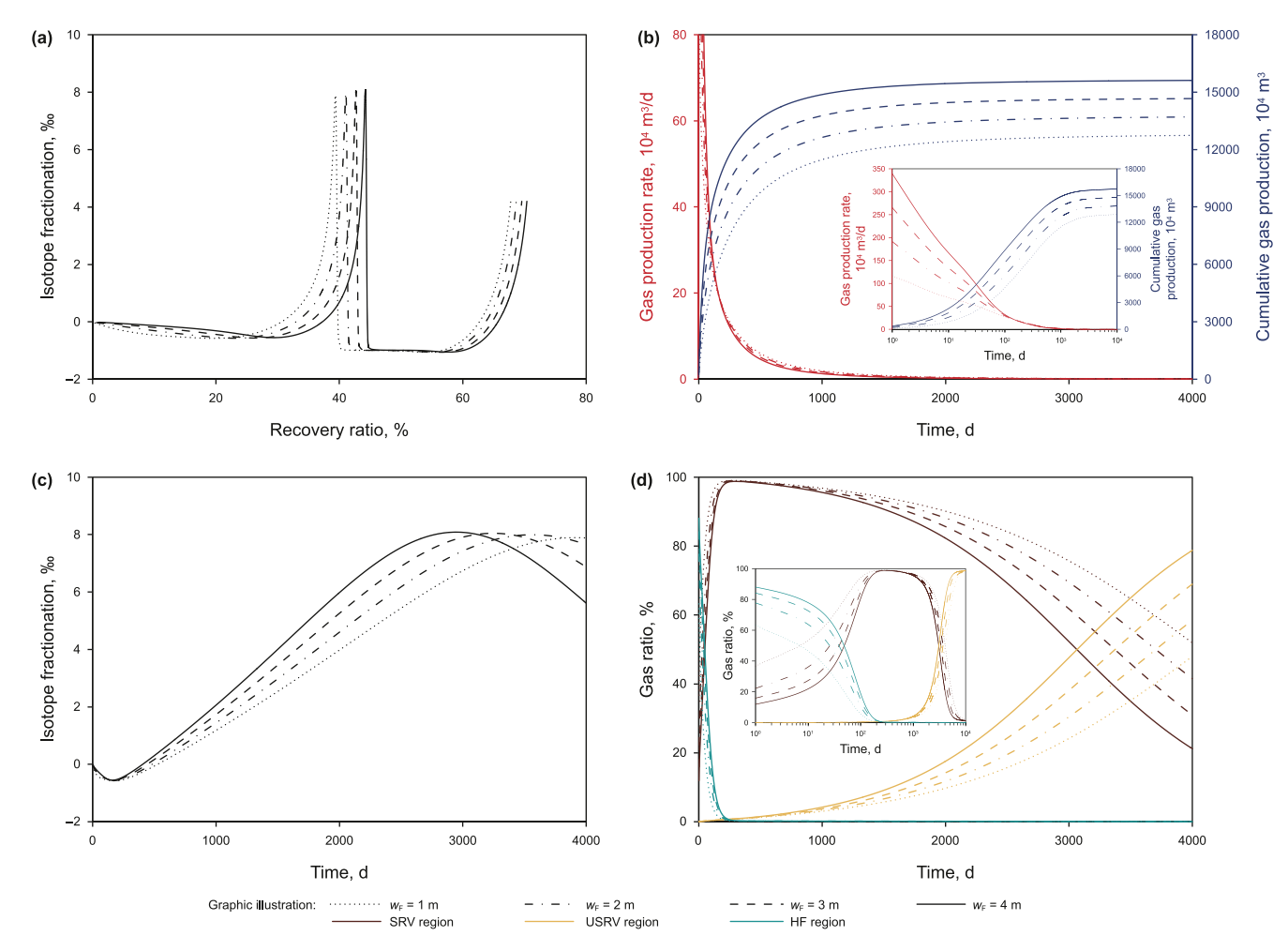


Fig. 10. Effect of w_F on isotope fractionation and gas production rate. The basic parameters are the same as in Fig. 8.

obvious phenomenon of "decrease first and then increase" during early production (Fig. 9(a) and (c)). The larger the $K_{\rm F}$, the faster the SRV region gas is depleted and the earlier the USRV region gas replenishment begins (Fig. 9(d)), and the earlier the "stable decrease again" feature of the isotope fractionation curve occurs in later production (Fig. 9(c)). The significance of $K_{\rm F}$ in gas production rate is evident; the higher the $K_{\rm F}$, the faster the gas production rate during early production, but the faster the reservoir capacity decreases; consequently, entering the stable low-production stage earlier (Fig. 9(b)).

(2) $w_{\rm F}$

 $w_{\rm F}$ is the width of the HF region. The effect of $w_{\rm F}$ on the isotope fractionation curves is similar to that of $K_{\rm F}$. During the early production, the greater the $w_{\rm F}$, the more pronounced the characteristic of the isotope fractionation curve being "decrease first and then increase" (Fig. 10(a)), and the earlier the characteristic of "stable decrease again" in isotope fractionation curve occurs during late production (Fig. 10(c)). The difference is that a larger $w_{\rm F}$ increases the volume of the HF region in the model, and because the porosity of the HF region is greater than that of the SRV and USRV regions ($\phi_{\rm F} > \phi_{\rm I} > \phi_{\rm O}$), the larger the $w_{\rm F}$, is the greater the total gas volume inside the reservoir, and the larger the cumulative gas production (Fig. 10(b)). Similarly, as the $w_{\rm F}$ increases, the recovery ratio corresponding to the "stable decrease again" of the isotope fractionation curve is higher.

The gas transport capacity of genuine hydraulic fractures under in situ conditions is also closely related to the complex architecture of the fracture network. Only simple slab fractures were considered in this study, and the ability of hydraulic fractures to transport gas was only affected by varying the apparent transport coefficient (K_F) and width (W_F) of the HF region. If we have access to micro-seismic data from shale gas wells, we would also like to introduce a more complex hydraulic fracture network system in future studies to investigate its implications on gas production rate and isotope fractionation.

3.3.3. Effect of USRV region related parameters

(1) D_0

 $D_{\rm O}$ is the diffusion coefficient of ¹²CH₄ molecule in USRV region. The larger the $D_{\rm O}$, the faster the USRV region gas is replenished, and the greater the ratio of USRV region gas in the total produced gas during late production (Fig. 11(d)), causing the "stable decrease again" of the isotope fractionation curve to occur earlier and the fractionation amplitude to decrease (Fig. 11(c)). The variation in $D_{\rm O}$ has little effect on the gas production rate and cumulative gas production curve, and an increase in $D_{\rm O}$ only slightly increases the cumulative gas production during late production (Fig. 11(b)).

(2) D_0*/D_0

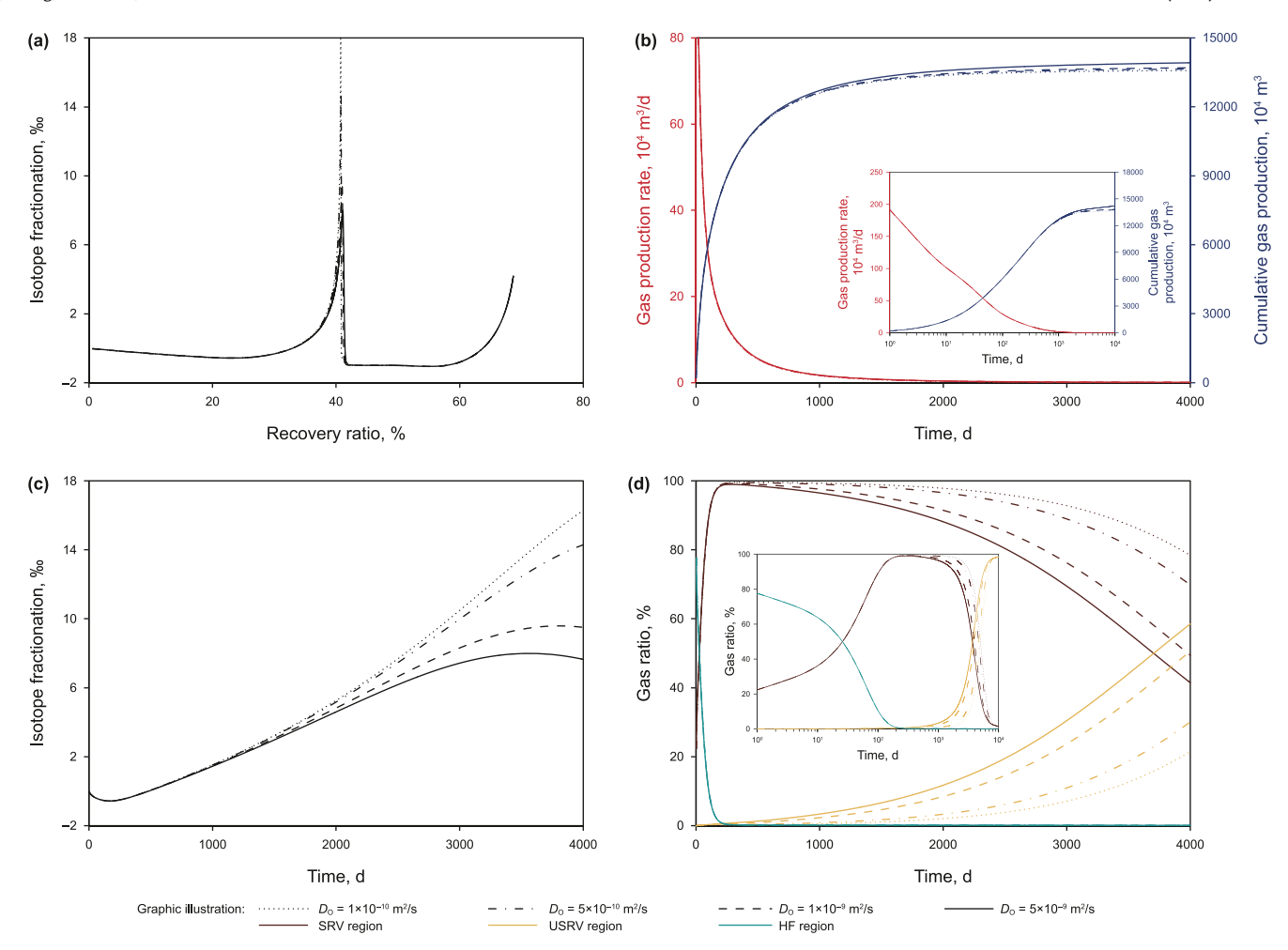


Fig. 11. Effect of D_0 on isotope fractionation and gas production rate. The basic parameters are the same as in Fig. 8.

 D_0^*/D_0 is the ratio of the $^{13}\mathrm{CH_4}$ to $^{12}\mathrm{CH_4}$ molecule diffusion coefficients in the USRV region. Similar to the impact of D^*/D on the gas production rate and isotope fractionation characteristics for a single gas transport region discussed in Section 3.1.1, a minor variation in D_0^*/D_0 has little effect on the gas production rate and gas ratio (Fig. 12(b) and (d)). The impact of D_0^*/D_0 on isotope fractionation is most pronounced during late production. The lower the D_0^*/D_0 , the weaker the relative diffusivity of $^{13}\mathrm{CH_4}$ molecules, the smaller the proportion of $^{13}\mathrm{CH_4}$ molecules produced concurrently during late production, the more negative the δ_{ins} , and the smaller the fractionation amplitude of the isotope fractionation curve (Fig. 12(a) and (c)).

4. Applications

4.1. General pattern of isotope fractionation during the shale gas production

Li et al. (2020a) discovered four isotope fractionation stages during shale core degassing. Through the above numerical simulations, we found that the same four-stage isotope fractionation exists in the shale gas production process, but the fractionation mechanism of each stage in the gas well production process is different from that of the core degassing process. Throughout the shale gas production process, there are four stages of isotope fractionation caused by gas transport: (1) seepage stage of the HF region gas, (2) transition stage between the HF region gas and SRV

region gas, (3) stable production stage of the SRV region gas, and (4) gas well depletion stage of the USRV region gas supply (Fig. 13). The gas transport mechanism and contribution of each gas transport region to the total gas produced varied at different fractionation stages. The monotonically decreasing characteristics of conventional production parameters (e.g., BHP and gas production rate) make it difficult to effectively identify distinct production stages. However, the four-stage characteristics of isotope fractionation during shale gas production offer a solution to the problem.

Stage 1 generally occurs during early production when the shale reservoir is hydraulically fractured and free gas within the HF region seepage under a large pressure difference (Fig. 13(a)). Because the scale of the hydraulic fracture, micro-fracture, and macro-pore in the HF region is much larger than the methane molecular diameter, the flow capacity of the $^{12}\mathrm{CH_4}$ and $^{13}\mathrm{CH_4}$ molecules is nearly equal ($K_F*/K_F\approx 1$), and no significant fractionation occurs at this stage (Fig. 13(b)). Ci et al. (2019) monitored the $\delta^{13}\mathrm{C_1}$ of well HG102 using the isotope logging technique, and the results showed no evident fractionation characteristics during early production, which was consistent with the fractionation characteristics of stage 1 (Fig. 13).

Stage 2 usually occurs during early or middle production, when the proportion of HF region gas in the produced gas gradually decreases, and as reservoir pressure decreases, the free and adsorbed gas in the SRV region begin to replenish (Fig. 13(d)). The SRV gas that is preferentially supplied enriches ¹²CH₄ because the ¹²CH₄ molecule has better diffusion capacity than the ¹³CH₄ molecule and

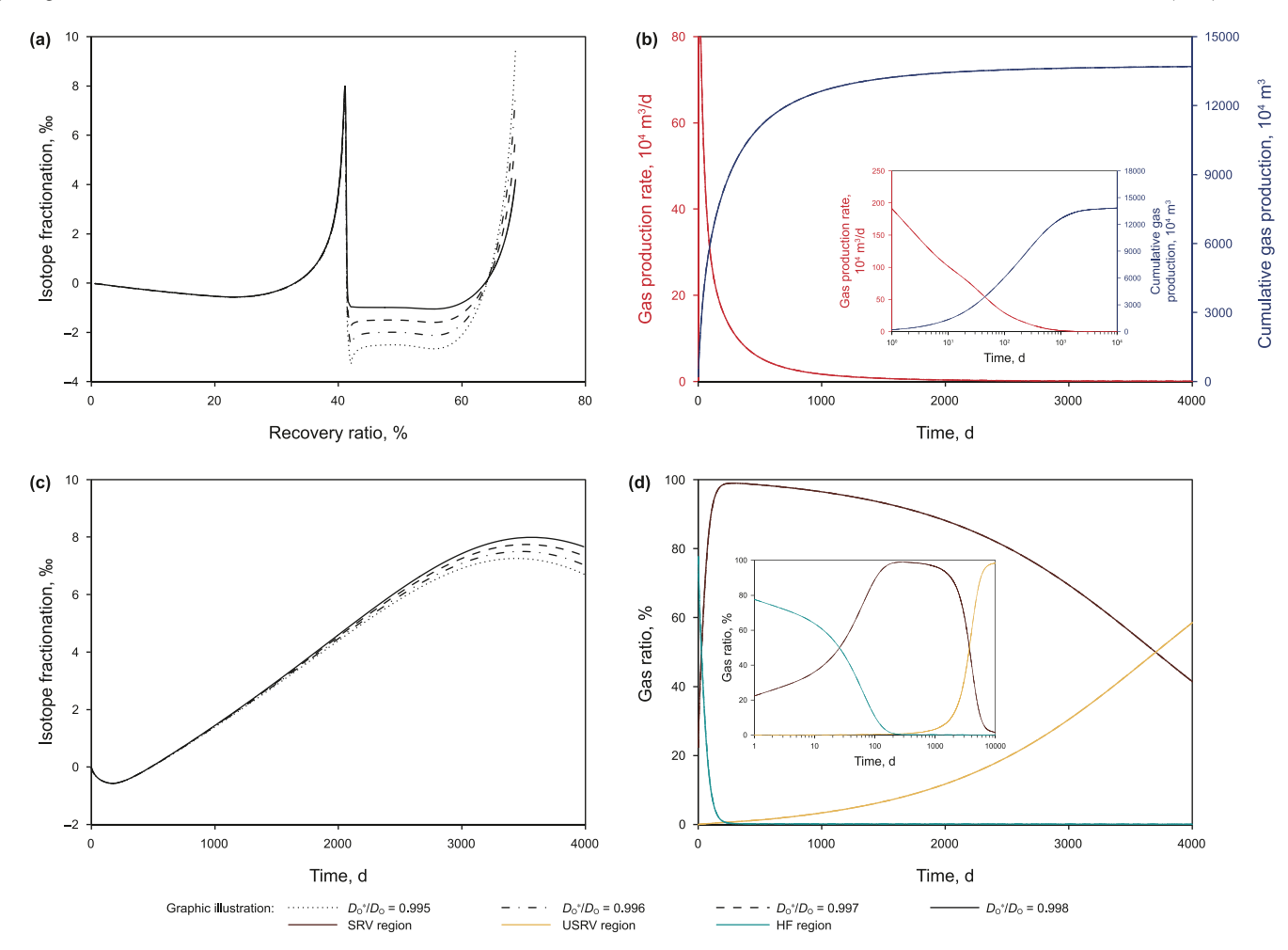


Fig. 12. Effect of D_0*/D_0 on isotope fractionation and gas production rate. The basic parameters are the same as in Fig. 8.

the $^{13}\text{CH}_4$ molecule is more easily adsorbed than the $^{12}\text{CH}_4$ molecule. As the proportion of SRV region gas to the total produced gas gradually increases, the $\delta^{13}\text{C}_1$ of the produced gas also starts to gradually become more negative (Fig. 13(e)). Zhao et al. (2022) conducted in situ monitoring of four shale gas wells in Sichuan Province, China, and also observed the fractionation pattern in which $\delta^{13}\text{C}_1$ continued to become more negative with production time during shale gas production (Fig. 13(f)). Similarly, Stage 2 was observed in the study conducted by Zhao et al. (2024).

Stage 3 normally occurs during middle or late production, when the HF region gas is basically depleted and the SRV region gas is the primary provider of the produced gas (Fig. 13(g)). A large number of free and adsorbed 12 CH₄ molecules of the SRV region have been output during stage 2, so it causes the adsorbed 13 CH₄ molecule in the matrix pores of the SRV region during stage 3 to begin to gradually desorb, and δ^{13} C₁ of produced gas starts to become consistently more positive as production time continues (Fig. 13(h)). Ci et al. (2019) also detected this phenomenon in the on-site δ^{13} C₁ monitoring data of well HG101-X2 (Fig. 13(i)).

Stage 4 would theoretically occur at the end of production. The $^{12}\text{CH}_4$ molecules in the USRV region are preferentially replenished as the reservoir pressure of SRV region lowers. The isotope fractionation curve exhibits a "stable decrease again" phenomenon (Fig. 13(k)) as the ratio of USRV region gas with negative $\delta^{13}\text{C}_1$ values in the produced gas gradually increases (Fig. 13(j)). However, due to the weak diffusion capacity of the gas in the USRV region, the gas production rate in Stage 4 is extremely low, and it is difficult to

develop shale gas wells at this stage of actual production for economic reasons. Nevertheless, Li et al (2020a) observed a "stable decrease again" phenomenon of $\delta^{13}C_1$ at the end of the degassing during laboratory degassing experiments on shale cores (Fig. 13(l)), attributing the cause to the output of gas in the kerogen pores inside the shale core under concentration differences.

Carbon isotope fractionation due to gas transport during a complete and continuous shale gas production process will exhibit the four stages described above. However, differences in the geological backgrounds, production methods, and fracturing effects of distinct production wells may result in the absence or fluctuation of a particular fractionation stage. For example, when the average pore size of the SRV region is large, resulting in a D_1*/D_1 close to 1, isotope fractionation may not occur, even after a long period of production. Shut-in on well measures during production may result in the reversal of $\delta^{13}C_1$ of produced gas into a new cycle (Li et al., 2022c). The poor fracturing results in a low ratio of HF region gas in the produced gas, making it difficult to observe the fractionation phenomenon in stages 1 and 2, and the $\delta^{13}C_1$ of the produced gas directly increases continuously during early production. The fractionation pattern of $\delta^{13}C_1$ during shale gas production is strongly linked to the diffusion and adsorption/desorption-related parameters of the reservoir, the BHP of shale gas wells, and the coupling effect of multi-scale gas transport regions. Besides the gas production rate, $\delta^{13}C_1$ is a sensitive indicator for the shale gas production process. We can better achieve shale gas well production

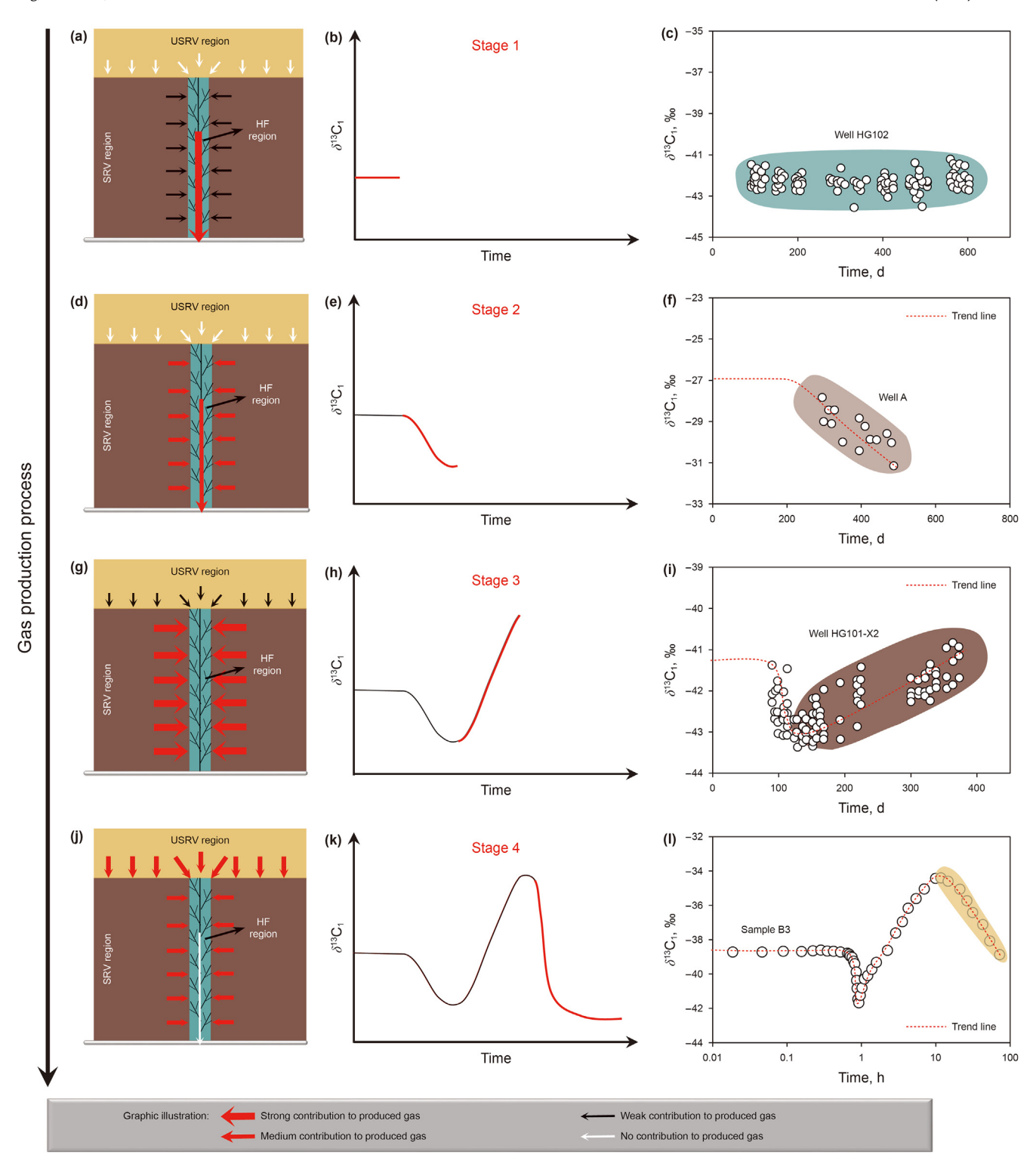


Fig. 13. Four stages of isotope fractionation during shale gas production. (Data in Fig. 13(c) and (i) are from Ci et al. (2019), data in Fig. 13(f) are from Zhao et al. (2022), and data in Fig. 13(l) are from Li et al. (2020a).

forecasting and adsorbed gas ratio evaluation during the production by using the sensitive and multi-stage isotope indicator.

4.2. Evaluation of the future performance of shale gas well

The Jiaoshiba, shale gas well YY6-2HF in China's Sichuan Basin was chosen to evaluate the practicality of the model established in

this study. Table 1 contains the basic data for the wells used in the analysis. In this section, the isotope fractionation model is applied to the history matching of field data and to evaluate the future performance of the shale gas well. Before applying the CIF model to production wells, we have partially validated the reliability of the model using previous experimental data (see Appendix C for details).

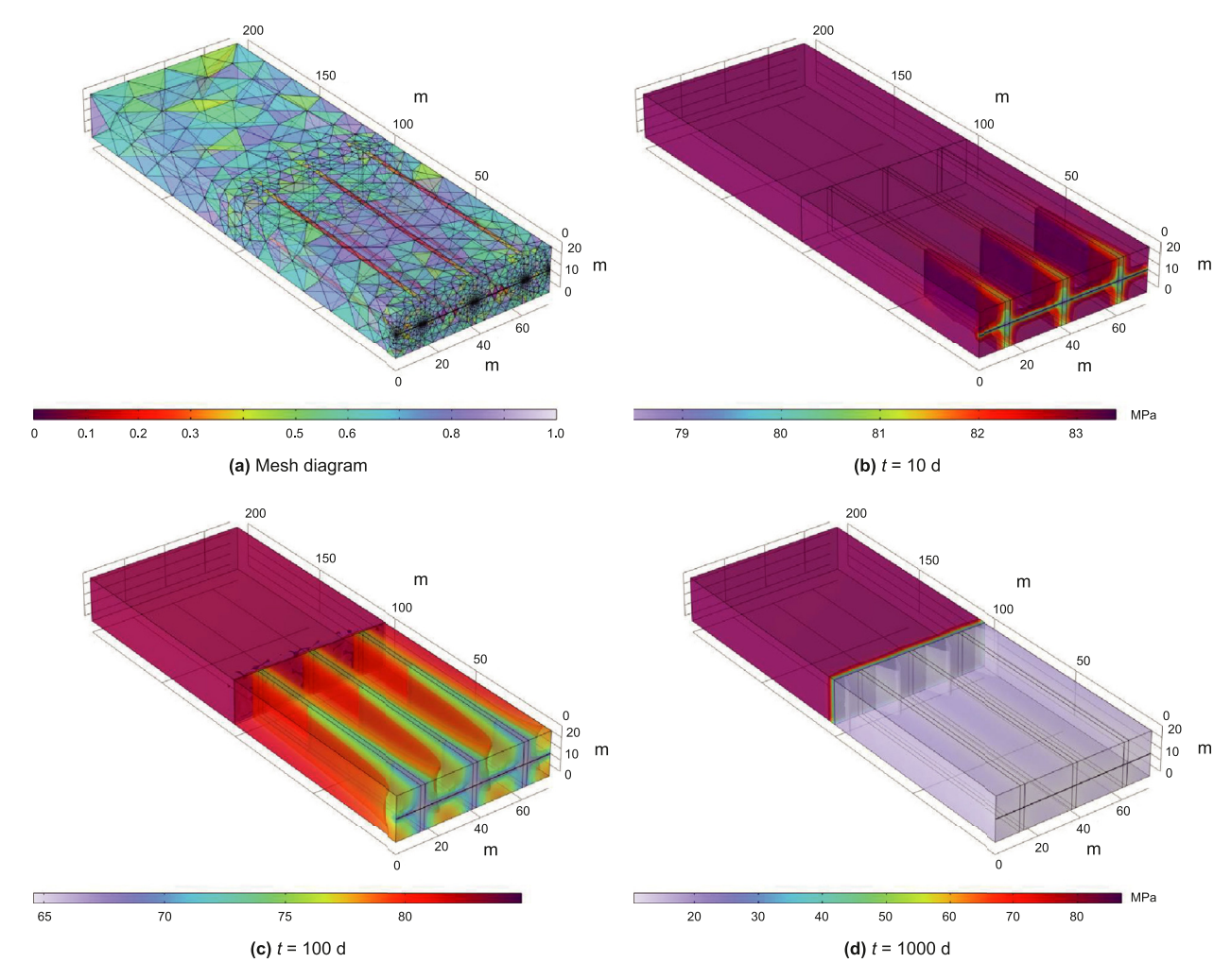


Fig. 14. Meshing and pressure evolution of shale reservoir.

A geometric model of the well YY6-2HF was established using basic construction parameters, and import governing equations, boundary conditions, and initial conditions for each region. The model is meshed (Fig. 14(a)) and the reservoir pressure field distribution can be obtained by numerically solving the nonlinear partial differential equations (PDEs) with the finite element method (FEM). The evolution of reservoir pressure shows that during early production, the pressure decline in the HF region mainly produces the HF region gas, with a small amount of SRV region gas produced (Fig. 14(b)). During middle production, the SRV region pressure decreases significantly, and the SRV region gas becomes the main contributor (Fig. 14(c)). During late production, there is no significant pressure difference between the SRV region and HF region, and the USRV region gas begins to diffuse through the pressure difference to the SRV and HF regions (Fig. 14(d)).

The exponential function is used to match the BHP data provided on-site in the first 2991 days, When the pressure decayed to 5 MPa, the production was maintained at a constant pressure of 5 MPa (Fig. 15(a)). The cumulative gas production, gas production rate, and isotope fractionation curves can be obtained by volume integration of the calculated pressure (P and P^*) and coverage (θ and θ^*) of 12 CH₄ and 13 CH₄ (see Appendix B for the calculation formula). The cumulative gas production curve, gas production rate curve, and isotope fractionation curve of the model were fitted with the field data, and the best fit was obtained by the BOBYQA

optimization algorithm to determine the diffusion-related parameters $(D_{\rm l}*/D_{\rm l},\ D_{\rm O}*/D_{\rm O})$, adsorption/desorption-related parameters $(V_{\rm L},\ P_{\rm L})$, and multi-scale gas transport regions-related parameters $(K_{\rm F},\ D_{\rm l},\ D_{\rm O},\ \phi_{\rm F},\ \phi_{\rm l},\ \phi_{\rm O})$ (Table 1). The calculated results of the model correspond with the field data (Fig. 15(b), (c), and (d)), demonstrating that our model can fit the cumulative gas production, gas production rate, and $\delta^{13}{\rm C}_{\rm l}$ data of a shale gas well simultaneously.

By substituting these historical fitting calibrated parameters into the model, we can calculate the EUR of free gas, adsorbed gas. and total EUR of well YY6-2 as 3.15×10^8 , 0.18×10^8 , and 3.33×10^8 m³, respectively (Fig. 16(a)). In the first, 1st, 5th, and 10th years, the adsorbed gas ratio during shale gas production were 1.65%, 10.03%, and 23.44%, respectively (Fig. 16(b)). In the later stage of production, the proportion of gas in the USRV region gradually increases (Fig. 16(c) and (d)), and the free gas in the distant matrix begins to supplement, so the free gas ratio begins to increase again in the 13.97th year (Fig. 16(b)). In Section 3.2, we learned that changes in bottom-hole flowing pressure (BHP) can have an impact on production and isotopic values of produced gas. The BHP of YY6-2HF decayed from 39.12 to 5 MPa in the first 2991 days, and then began production at a constant pressure of 5 MPa. Due to the sudden change in BHP on the 2991th day, the corresponding gas ratio was also affected (Fig. 16(d)). This model is applicable to shale gas wells where significant methane carbon isotope fractionation can be observed and long shut-in periods are absent.

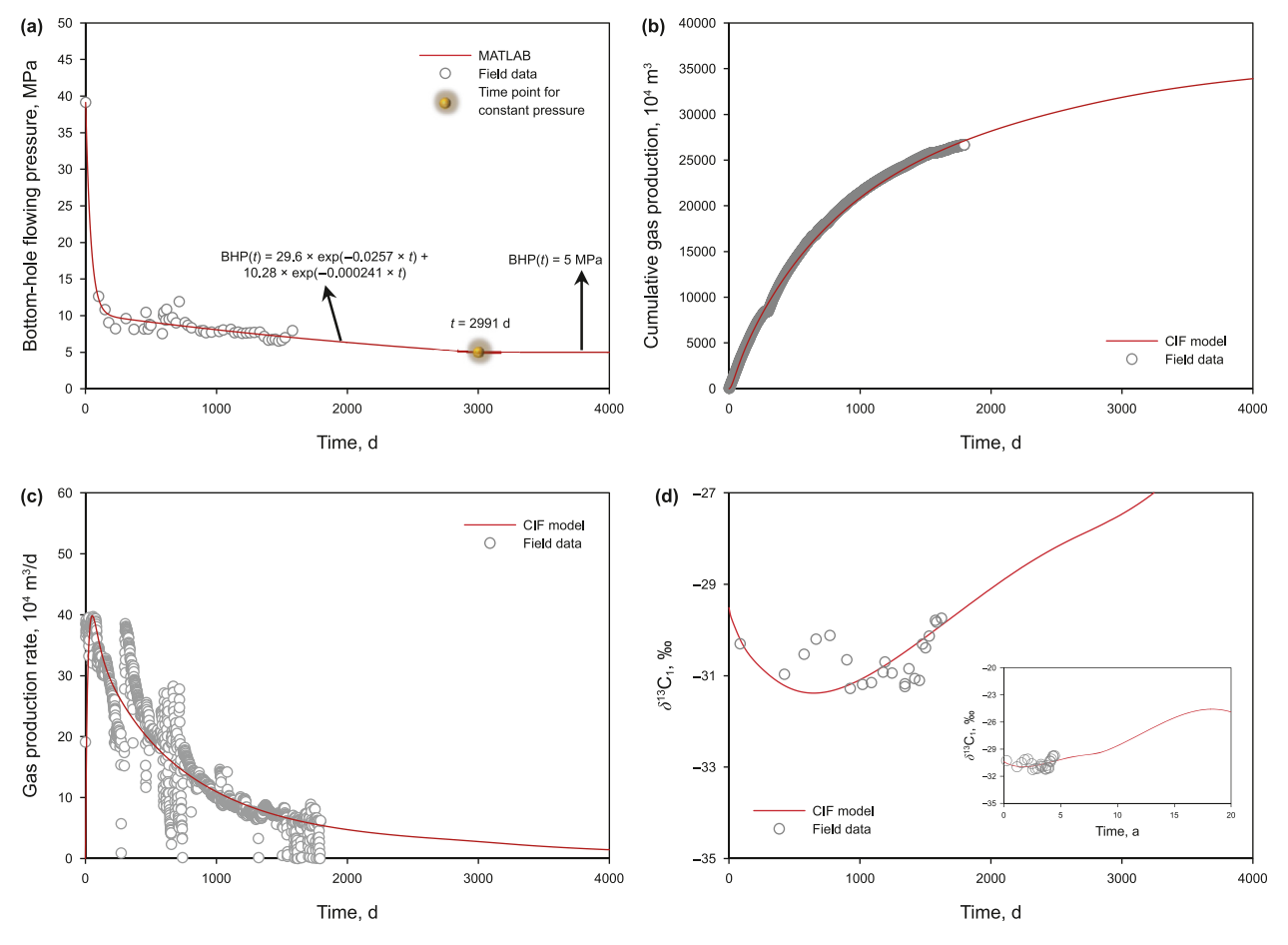


Fig. 15. History match of cumulative gas production, gas production rate, and $\delta^{13}C_1$ of Well YY6-2HF.

5. Conclusions

In this research, we proposed a three-dimensional continuous flow equation for $^{12}\mathrm{CH_4}$ and $^{13}\mathrm{CH_4}$ based on previous studies, established an isotope fractionation model applicable to the production process in shale gas wells for the first time, and quantitatively revealed the isotope fractionation mechanism during shale gas production. Based on parameter sensitivity analysis, on-site $\delta^{13}\mathrm{C_1}$ data monitoring, and specific case studies, the key findings can be summed up as follows:

- (1) Field monitoring $\delta^{13}C_1$ data show an obvious isotope fractionation phenomenon during shale gas well production, which is governed by the diffusion-adsorption/desorption effect of gas, the bottom-hole flowing pressure (BHP) of the gas well, and the multi-scale gas transport regions coupling of the reservoir. Variation diffusion-adsorption/desorption parameters affect the fractionation amplitude of isotope fractionation curves, shift in BHP will cause fluctuations in isotope fractionation curves, and coupling of multi-scale gas transport regions is the main reason for the four stages of the isotope fractionation curve during shale gas production.
- (2) The order of the factors that govern isotope fractionation during gas diffusion and adsorption/desorption is $D^*/D > P_L > V_L > \alpha >$ others. A small average pore size (D^*/D) of the matrix, strong rock adsorption capacity (P_L) , high maximum adsorbed gas volume (V_L) , and large fractionation

- factor between the adsorbate phase and gas phase (α) will all result in more obvious isotope fractionation phenomena.
- (3) In addition to diffusion and adsorption/desorption related parameters, the BHP and gas production rate are intimately related to isotope fractionation during shale gas production. The attenuation way of BHP will affect the amplitude of isotope fractionation and the decreasing rate of gas production rate. Under the condition of constant BHP and no other regional gas replenishment, isotope fractionation curve and the gas production rate curve exhibit opposite trends as production progresses, and as the fractionation amplitude of the isotope fractionation curve increases, the gas production rate decreases and the gas well approaches depletion.
- (4) Isotope fractionation caused by gas transport in a complete and continuous shale gas production process will be characterized by four stages of fractionation: the seepage stage of HF region gas, the transition stage between HF region gas and SRV region gas, the stable production stage of SRV region gas, and the gas well depletion stage of the USRV region gas supply. The coupling of multi-scale gas transport regions (HF, SRV, and USRV regions) and the superposition of multimechanism (seepage, diffusion, and adsorption/desorption) in shale reservoirs resulted in the formation of four stages of isotope fractionation.
- (5) By combining geological and construction parameters, we applied the isotope fractionation model to a well in the Jiaoshiba area of Sichuan, China, and conducted production

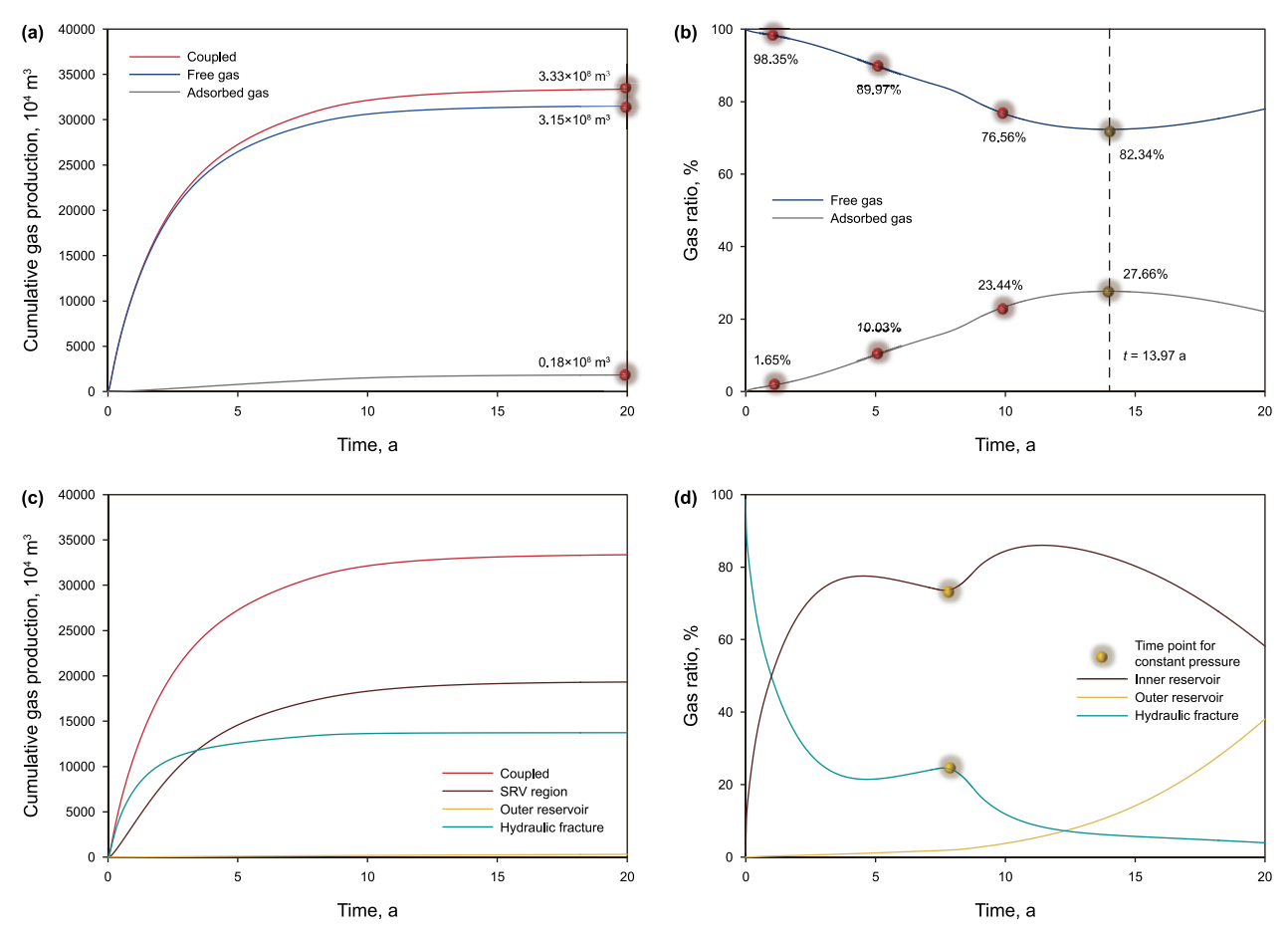


Fig. 16. Production prediction and evaluation of adsorbed/free gas ratio during production of well YY6-2HF.

prediction and adsorption gas ratio evaluation. According to the research findings, the EUR of the well is $3.33 \times 10^8 \, \mathrm{m}^3$, and the adsorbed gas ratio during shale gas production were 1.65%, 10.03%, and 23.44% in the 1st, 5th, and 10th, respectively.

These findings offer a theoretical comprehension of gas migration under in-situ conditions, production evaluation of shale gas wells, and isotope fractionation phenomenon in on-site monitoring. Nevertheless, future studies should consider the coexistence of multiple gas transport mechanisms and the impact of complex discrete fracture geometries on isotope fractionation. To extend this

Table 1Parameters used for and obtained from the model calibration.

Parameters	Value	Source
The thick of the reservoir (h), m ³	20	Fang (2017)
The length of the horizontal well (l) , m^3	1447	Fang (2017)
The radius of the horizontal well (r_w) , m	0.1	Fang (2017)
Spacing between the HF region, m	32.82	Fang (2017)
Rock density ($\rho_{\rm rock}$), g/cm ³	2.6	Fang (2017)
Initial reservoir pressure (P_0) , MPa	39.12	Fang (2017)
Reservoir temperature (<i>T</i>), °C	85.99	Fang (2017)
The length of HF region (l), m	200.05	Optimize calibration
Width of the HF region (w_F) , m	5.30	Optimize calibration
The porosity of HF region $(\phi_{\rm F})$	28.11%	Optimize calibration
The porosity of SRV region (ϕ_I)	6.91%	Optimize calibration
The porosity of USRV region (ϕ_0)	7.22%	Optimize calibration
Transport coefficient of HF region (K_F) , m ² /s	1.61×10^{-4}	Optimize calibration
Diffusion coefficient of SRV region (D_I) , m^2/s	8.53×10^{-8}	Optimize calibration
Diffusion coefficient of USRV region (D_0) , m ² /s	7.54×10^{-10}	Optimize calibration
Langmuir volume (V_L), cm ³ /g	2.48	Optimize calibration
Langmuir pressure (P_L), MPa	3.137	Optimize calibration
D_1^*/D_1	0.998	Optimize calibration
D_0^*/D_0	0.9	Optimize calibration
$\delta^{13}C_1$ ($t=0$), δ_0	-30.34‰	Optimize calibration

model to coalbed methane wells, the influence of adsorption layers on porosity and the effects of gas-water two-phase flow on isotope fractionation must also be accounted for.

Nomenclature

ϕ_{F}	The porosity of the HF region, dimensionless	ϕ_{I}	The porosity of the SRV region, dimensionless
$\phi_{\rm O}$	The porosity of the USRV region, dimensionless	$P_{\rm F}$	The pressure of the ¹² CH₄ in the HF region, Pa
$P_{\rm I}$	The pressure of the ¹² CH ₄ in the SRV region, Pa	$P_{\rm O}$	The pressure of the ¹² CH ₄ in the USRV region, Pa
$K_{\rm F}$	The apparent transport coefficient of the HF region, m ² /s	D	The diffusion coefficient in matrix pore
$D_{\rm O}$	The diffusion coefficient in the USRV region	D_{I}	The diffusion coefficient in the SRV region
ρ_{rock}	The apparent rock density, g/cm ³	C	Mass balance ratio ($\rho_{\text{rock}}V_LZRT/V_{\text{std}}$, Pa)
K	Langmuir constant, Pa ⁻¹	$V_{\rm L}$	The utmost amount of gas that can be adsorbed per unit mass of rock, cm ³ /g
T	Reservoir temperature, K	R	The ideal gas constant, $8.314 \mathrm{I mol^{-1} K^{-1}}$
$P_{\rm wf}$	Bottom-hole flowing pressure (BHP), Pa	$V_{\rm m}$	The molar volume constant of the gas standard condition, 0.0224 m ³ /mol
$R_{\rm st}$	Carbon isotope atomic ratio of the PDB standard samples, 0.0112372	δ_0	Initial carbon isotopic value
$r_{\rm w}$	Radius of the horizontal well, m	1	Half-length of the HF region, m
h	The thick of the reservoir	$w_{\rm F}$	Width of the HF region, m
$D_{\rm I}^*/D_{\rm I}$	Ratio of diffusion coefficients of 12CH4 and 12CH4 in SRV region	D_0*/D_0	Ratio of diffusion coefficients of ¹² CH ₄ and ¹² CH ₄ in USRV region
C	Gas concentration of the matrix pore, mol/m ³	P_0	Initial reservoir pressure, Pa
$n_{\rm free}$	The mole of free gas, mol	$n_{\rm ads}$	The mole of adsorbed gas, mol
α	The fractionation factor between the adsorbate and gas phase	$\overrightarrow{\nu}_{F}$	The Darcy velocity vector of gas in the HF region, m/s
P	The internal pressure in the matrix pore	μ_{g}	The viscosity of gas, Pa•s
Z	The gas compressibility factor	$V_{\text{reservoir}}$	The volume of rock, m ³
θ	The fractional coverage of adsorbed gas	φ	The porosity of matrix pore
$q_{ m source}$	Mass source, kg/m³/s	F _X	Flux in the <i>x</i> -direction, mol•m ⁻² s ⁻¹
k _F	The permeability of HF region, m ²	$q_{ m sink}$	Mass sink, kg/m ³ /s

CRediT authorship contribution statement

Jun Wang: Writing — original draft, Visualization, Validation, Software, Methodology, Investigation, Formal analysis, Data curation, Conceptualization. Fang-Wen Chen: Project administration, Funding acquisition. Wen-Biao Li: Writing — review & editing, Supervision, Resources, Project administration, Methodology, Funding acquisition, Formal analysis, Conceptualization. Shuang-Fang Lu: Writing — review & editing, Resources, Project administration, Methodology, Funding acquisition, Conceptualization. Sheng-Xian Zhao: Project administration, Investigation, Funding acquisition. Yong-Yang Liu: Investigation, Data curation. Zi-Yi Wang: Investigation, Data curation.

Data availability

Data and model will be made available on request.

Declaration of interests

The authors declare the following financial interests/personal relationships which may be considered as potential competing interests: The authors declare that they have no known competing financial interests or personal relationships that could have appeared to influence the work reported in this paper.

Acknowledgments

This work was supported by the Natural Science Foundation of China (Grant No. 42302170), National Postdoctoral Innovative Talent Support Program (Grant No. BX20220062), CNPC Innovation Found (Grant No. 2022DQ02-0104), National Science Foundation of Heilongjiang Province of China (Grant No. YQ2023D001), Postdoctoral Science Foundation of Heilongjiang Province of China (Grant No. LBH-Z22091), the Natural Science Foundation of Shandong Province (Grant No. ZR2022YQ30).

Appendix A. Derivation of the governing equations for each region

A.1. Derivation of the governing equation for the SRV and USRV region

The three-dimensional continuous flow equation for 12 CH $_4$ and 13 CH $_4$ is

$$\begin{cases} (C_1 B_2 - C_2 B_1) \frac{\partial P}{\partial t} = \nabla \cdot (B_2 D \nabla P - B_1 D^* \nabla P^*) \\ (C_1 B_2 - C_2 B_1) \frac{\partial P^*}{\partial t} = \nabla \cdot (C_1 D^* \nabla P^* - C_2 D \nabla P) \end{cases}$$
(A1.1)

with

$$\begin{cases} B_{1} = -\frac{(1-\phi)cKK^{*}P}{(1+KP+K^{*}P^{*})^{2}} \\ C_{1} = \phi + \frac{(1-\phi)c(K+KK^{*}P^{*})}{(1+KP+K^{*}P^{*})^{2}} \\ B_{2} = \phi + \frac{(1-\phi)c(K^{*}+KK^{*}P)}{(1+KP+K^{*}P^{*})^{2}} \\ C_{2} = -\frac{(1-\phi)cKK^{*}P^{*}}{(1+KP+K^{*}P^{*})^{2}} \end{cases}$$
(A1.2)

The following is the derivation process of Eqs. (A1.1) and (A1.2). From the continuity equation (first considering the simple one-dimensional equation), we obtain

$$\frac{\partial C}{\partial t} = -\frac{\partial F_X}{\partial x} \tag{A1.3}$$

where *C* is gas concentration of the matrix pore, mol/m³; and F_x is flux in the *x*-direction, mol·m⁻² s⁻¹. Considering that the matrix pores contain free gas and adsorbed gas, Eq. (A1.3) becomes:

$$\frac{\partial C_{\text{free}}}{\partial t} + \frac{\partial C_{\text{ads}}}{\partial t} = -\frac{\partial F_{X}}{\partial x} \tag{A1.4}$$

Based on the gas equation of state (EOS) and Langmuir isothermal adsorption model, $C_{\rm free}$ and $C_{\rm ads}$ indicate that

$$C_{\text{free}} = \frac{n_{\text{free}}}{V_{\text{reservoir}}} = \frac{P(V_{\text{reservoir}}\phi)/ZRT}{V_{\text{reservoir}}} = \phi \frac{P}{ZRT}$$
(A1.5)

and

$$\begin{split} C_{ads} = & \frac{n_{ads}}{V_{reservoir}} = \frac{(V_L \theta)(\rho_{rock} V_{reservoir} (1 - \phi))/V_m}{V_{reservoir}} \\ = & (1 - \phi) \frac{V_L \rho_{rock}}{V_m} \theta \end{split} \tag{A1.6}$$

where $n_{\rm free}$ is the mole of free gas, mol; $V_{\rm reservoir}$ is the volume of rock, m³; P is internal pressure in the matrix pore, Pa; ϕ is the porosity of matrix pore; Z is gas compressibility factor; R is the ideal gas constant, 8.314 J mol $^{-1}$ K $^{-1}$; T is the reservoir temperature, K; $n_{\rm ads}$ is mole of adsorbed gas, mol; $V_{\rm L}$ is Langmuir volume, m 3 /kg; θ is the fractional coverage of adsorbed gas; $\rho_{\rm rock}$ is the density of rock, kg/m 3 ; $V_{\rm m}$ is the molar volume constant of the gas standard condition, 0.0224 m 3 /mol.

Among the above parameters, t and x are independent variables, P, θ , and F_x are dependent variables, while the rest of the parameters are constants independent of position and time. Substituting Eqs. (A1.5) and (A1.6) into Eq. (A1.4) we get

$$\frac{\phi}{ZRT} \frac{\partial P}{\partial t} + (1 - \phi) \frac{V_{L} \rho_{rock}}{V_{m}} \frac{\partial \theta}{\partial t} = -\frac{\partial F_{x}}{\partial x}$$
(A1.7)

Multiply both sides of equation (A1.7) by $\it ZRT$ simultaneously, and we get

$$\phi \frac{\partial P}{\partial t} + (1 - \phi) \frac{V_L \rho_{\text{rock}} ZRT}{V_m} \frac{\partial \theta}{\partial t} = -\frac{\partial F_X}{\partial x} ZRT$$
 (A1.8)

From Fick's first law in porous media, it follows that

$$F_{\rm X} = -\frac{D}{\phi} \frac{\partial C(x)}{\partial x} \tag{A1.9}$$

where D is the diffusion coefficient, m^2/s ; substituting Eq. (A1.9) into Eq. (A1.8) we get

$$\phi \frac{\partial P}{\partial t} + (1 - \phi) \frac{V_{L} \rho_{rock} ZRT}{V_{m}} \frac{\partial \theta}{\partial t} = \frac{\partial}{\partial x} \left(\frac{D}{\phi} \frac{\partial C}{\partial x} \right) ZRT$$
(A1.10)

The change in concentration is caused by the free gas flowing in and out along the *x*-direction. Thus, we have

$$C = \frac{n}{V_{\text{reservoir}}} = \frac{PV_{\text{rock}}\phi/ZRT}{V_{\text{reservoir}}} = \frac{P\phi}{ZRT}$$
(A1.11)

Substituting Eq. (A1.11) into Eq. (A1.10) we get

$$\phi \frac{\partial P}{\partial t} + (1 - \phi) \frac{V_{L} \rho_{\text{rock}} ZRT}{V_{m}} \frac{\partial \theta}{\partial t} = \frac{\partial}{\partial x} \left(D \frac{\partial P}{\partial x} \right)$$
(A1.12)

Here, we set a constant c [$c = (\rho_{\text{rock}}V_{\text{L}}ZRT)/V_{\text{m}}$], and Eq. (A1.12) becomes:

$$\phi \frac{\partial P}{\partial t} + (1 - \phi)c \frac{\partial \theta}{\partial t} = \frac{\partial}{\partial x} \left(D \frac{\partial P}{\partial x} \right)$$
 (A1.13)

If continuous flow is considered in three dimensions, Eq. (A1.13) becomes:

$$\phi \frac{\partial P}{\partial t} + (1 - \phi)c \frac{\partial \theta}{\partial t} = \frac{\partial}{\partial x} \left(D_x \frac{\partial P}{\partial x} \right) + \frac{\partial}{\partial y} \left(D_y \frac{\partial P}{\partial y} \right) + \frac{\partial}{\partial z} \left(D_z \frac{\partial P}{\partial z} \right)$$
(A1.14)

In this model, we do not consider the heterogeneity of the reservoir and assume that the gas diffusion coefficient is the same in all directions, we have

$$\phi \frac{\partial P}{\partial t} + (1 - \phi)c \frac{\partial \theta}{\partial t} = \nabla \cdot (D\nabla P)$$
 (A1.15)

The three-dimensional continuous flow equation for $^{12}\text{CH}_4$ and $^{13}\text{CH}_4$ is

$$\begin{cases} \phi \frac{\partial P}{\partial t} + (1 - \phi)c \frac{\partial \theta}{\partial t} = \nabla \cdot (D \nabla P) \\ \phi \frac{\partial P^*}{\partial t} + (1 - \phi)c \frac{\partial \theta^*}{\partial t} = \nabla \cdot (D^* \nabla P^*) \end{cases}$$
(A1.16)

To homogenise the independent variables into pressure, we introduced the theory of isotopic competitive adsorption (Xia and Tang, 2012):

$$\begin{cases} \theta = \frac{KP}{1 + KP + K^*P^*} \\ \theta^* = \frac{K^*P^*}{1 + KP + K^*P^*} \end{cases}$$
(A1.17)

where K is the Langmuir coefficient, Pa^{-1} . The connection between K^* and K can be determined using statistical thermodynamics:

$$\ln\left(\frac{K^*}{K}\right) = A/T^2 - B/T \tag{A1.18}$$

where $A = 95.17 K^2$ is for the isotope fractionation of $^{12}\text{CH}_4$ and $^{13}\text{CH}_4$, and B = 0.125 K is calculated from the experimental data by Bruner et al. (1966).

Taking partial derivatives of both sides of the equal sign of Eq. (A1.17) with respect to time we obtain:

$$\begin{cases} \frac{\partial \theta}{\partial t} = \frac{K \frac{\partial P}{\partial t} + KK^* P^* \frac{\partial P}{\partial t} - KK^* P \frac{\partial P^*}{\partial t}}{(1 + KP + K^* P^*)^2} \\ \frac{\partial \theta^*}{\partial t} = \frac{K^* \frac{\partial P^*}{\partial t} + KK^* P \frac{\partial P^*}{\partial t} - KK^* P^* \frac{\partial P}{\partial t}}{(1 + KP + K^* P^*)^2} \end{cases}$$
(A1.19)

Substituting Eq. (A1.19) into Eq. (A1.17) we have

$$\begin{cases} \phi \frac{\partial P}{\partial t} + (1 - \phi)c \frac{K \frac{\partial P}{\partial t} + KK^* P^* \frac{\partial P}{\partial t} - KK^* P \frac{\partial P^*}{\partial t}}{(1 + KP + K^* P^*)^2} = \nabla \cdot (D\nabla P) \\ \phi \frac{\partial P^*}{\partial t} + (1 - \phi)c \frac{K^* \frac{\partial P^*}{\partial t} + KK^* P \frac{\partial P^*}{\partial t} - KK^* P^* \frac{\partial P}{\partial t}}{(1 + KP + K^* P^*)^2} = \nabla \cdot (D^* \nabla P^*) \\ \cdot (A1.12) \end{cases}$$

$$(A1.12)$$

Combining similar terms for Eq. (A1.20) we obtain:

$$\begin{cases} \left[\phi + \frac{(1 - \phi)c(K + KK^*P^*)}{(1 + KP + K^*P^*)^2} \right] \frac{\partial P}{\partial t} - \frac{(1 - \phi)cKK^*P}{(1 + KP + K^*P^*)^2} \frac{\partial P^*}{\partial t} = \nabla \cdot (D\nabla P) \\ \left[\phi + \frac{(1 - \phi)c(K^* + KK^*P)}{(1 + KP + K^*P^*)^2} \right] \frac{\partial P^*}{\partial t} - \frac{(1 - \phi)cKK^*P^*}{(1 + KP + K^*P^*)^2} \frac{\partial P}{\partial t} = \nabla \cdot (D^*\nabla P^*) \end{cases}$$
(A1.21)

To make the equation more concise we introduce four constants:

$$\begin{cases} B_{1} = -\frac{(1-\phi)cKK^{*}P}{(1+KP+K^{*}P^{*})^{2}} \\ C_{1} = \phi + \frac{(1-\phi)c(K+KK^{*}P^{*})}{(1+KP+K^{*}P^{*})^{2}} \\ B_{2} = \phi + \frac{(1-\phi)c(K^{*}+KK^{*}P)}{(1+KP+K^{*}P^{*})^{2}} \\ C_{2} = -\frac{(1-\phi)cKK^{*}P^{*}}{(1+KP+K^{*}P^{*})^{2}} \end{cases}$$
(A1.22)

Substitute B_1 , C_1 , B_2 and C_2 into Eq. (A1.21), we have

$$\begin{cases} C_1 \frac{\partial P}{\partial t} + B_1 \frac{\partial P^*}{\partial t} = \nabla \cdot (D \nabla P) \\ B_2 \frac{\partial P^*}{\partial t} + C_2 \frac{\partial P}{\partial t} = \nabla \cdot (D^* \nabla P^*) \end{cases}$$
(A1.23)

With a slight transformation of Eq. (A1.22), we obtain the final three-dimensional continuous flow equations for ¹²CH₄ and ¹³CH₄:

$$\begin{cases} (C_1 B_2 - C_2 B_1) \frac{\partial P}{\partial t} = \nabla \cdot (B_2 D \nabla P - B_1 D^* \nabla P^*) \\ (C_1 B_2 - C_2 B_1) \frac{\partial P^*}{\partial t} = \nabla \cdot (C_1 D^* \nabla P^* - C_2 D \nabla P) \end{cases}$$
(A1.24)

So, the governing equation of SRV region is

$$\begin{cases} (C_{1_I}B_{2_I} - C_{2_I}B_{1_I}) \frac{\partial P_I}{\partial t} = \nabla \cdot (B_{2_I}D_I \nabla P_I - B_{1_I}D_I^* \nabla P_I^*) \\ (C_{1_I}B_{2_I} - C_{2_I}B_{1_I}) \frac{\partial P_I^*}{\partial t} = \nabla \cdot (C_{1_I}D_I^* \nabla P_I^* - C_{2_I}D_I \nabla P_I) \end{cases}$$
(A1.25)

with

$$\begin{cases} B_{1_I} = -\frac{(1 - \phi_I)cKK^*P_I}{(1 + KP_I + K^*P_I^*)^2} \\ C_{1_I} = \phi_I + \frac{(1 - \phi_I)c(K + KK^*P_I^*)}{(1 + KP_I + K^*P_I^*)^2} \\ B_{2_I} = \phi_I + \frac{(1 - \phi_I)c(K^* + KK^*P_I)}{(1 + KP_I + K^*P_I^*)^2} \\ C_{2_I} = -\frac{(1 - \phi_I)cKK^*P_I^*}{(1 + KP_I + K^*P_I^*)^2} \end{cases}$$
(A1.26)

The governing equation of USRV region is

$$\begin{cases} (C_{1_0}B_{2_0} - C_{2_0}B_{1_0}) \frac{\partial P_0}{\partial t} = \nabla \cdot (B_{2_0}D_0\nabla P_0 - B_{1_0}D_0^*\nabla P_0^*) \\ (C_{1_0}B_{2_0} - C_{2_0}B_{1_0}) \frac{\partial P_0^*}{\partial t} = \nabla \cdot (C_{1_0}D_0^*\nabla P_0^* - C_{2_0}D_0\nabla P_0) \end{cases}$$
(A1.27)

with

$$\begin{cases} B_{1-0} = -\frac{(1-\phi_0)cKK^*P_0}{(1+KP_0+K^*P_0^*)^2} \\ C_{1-0} = \phi_0 + \frac{(1-\phi_0)c(K+KK^*P_0^*)}{(1+KP_0+K^*P_0^*)^2} \\ B_{2-0} = \phi_0 + \frac{(1-\phi_0)c(K^*+KK^*P_0)}{(1+KP_0+K^*P_0^*)^2} \end{cases}$$

$$C_{2-0} = -\frac{(1-\phi_0)cKK^*P_0^*}{(1+KP_0+K^*P_0^*)^2}$$

A.2. Derivation of the regional governing equation for HF region

In this section, by drawing inspiration from the Ozkan trilinear flow model (Ozkan et al., 2011), the hydraulic fracture network system is considered as an equivalent high permeability flow region composed of the fracture network and nearby matrix. Considering the seepage effect of free gas in hydraulic fracturing, the PDEs for the transport of ¹²CH₄ and ¹³CH₄ molecules in the HF region are as follows:

$$\begin{cases} \phi_{F} \frac{\partial P_{F}}{\partial t} = K_{F} \nabla^{2} P_{F} \\ \phi_{F} \frac{\partial P_{F}^{*}}{\partial t} = K_{F} \nabla^{2} P_{F}^{*} \end{cases}$$
(A2.1)

The following is the derivation process of Eq. (A2.1).

The gas mass balance equation for the HF region can be expressed as (Hu et al., 2022)

$$\frac{\partial(\rho_{F}\phi_{F})}{\partial t} + \nabla \cdot \left(\rho_{F}\overrightarrow{\nu}_{F}\right) = q_{\text{source}} - q_{\text{sink}}$$
(A2.2)

where \overrightarrow{v}_F is the Darcy velocity vector of gas in the HF region, m/s; q_{source} is the mass source, that is, the intensity of the source per unit volume delivered by the matrix region to the HF region, kg/m³/s; q_{sink} is the mass sink, that is, the intensity of the sink per unit volume delivered by the HF region to the matrix region, kg/m³/s; the subscript F denotes HF region. The Darcy velocity vector in the HF region is expressed as follows:

$$\overrightarrow{v}_{F} = -\frac{k_{F}}{\mu_{\sigma}} \nabla P_{F} \tag{A2.3}$$

where $k_{\rm F}$ is the permeability of HF region, m²; $\mu_{\rm g}$ is the viscosity of gas, Pa·s; $\nabla P_{\rm F}$ is the pressure gradient inside the HF region, Pa·m⁻¹. From the gas equation of state, we obtain:

$$\rho_{\rm F} = \frac{M}{RT} \left(\frac{P_{\rm F}}{Z} \right) \tag{A2.4}$$

Substituting Eqs. (A2.3) and (A2.4) into Eq. (A2.2), we obtain:

$$\frac{\partial}{\partial t} \left(\frac{M}{RT} \frac{P_F}{Z} \phi_F \right) - \nabla \cdot \left(\frac{M}{RT} \frac{P_F}{Z} \frac{k_F}{\mu_g} \nabla P_F \right) = q_{\text{source}} - q_{\text{sink}}$$
 (A2.5)

Using the continuous boundary condition, we can determine the source and sink terms. Then we get

$$\frac{\partial}{\partial t} \left(\frac{M}{RT} \frac{P_F}{Z} \phi_F \right) - \nabla \cdot \left(\frac{M}{RT} \frac{P_F}{Z} \frac{k_F}{\mu_g} \nabla P_F \right) = 0 \tag{A2.6}$$

In this model, M, R, and T are considered constants. k_F , Z and μ_g both are functions of the actual gas pressure P. Therefore, Eq. (A2.6) is a nonlinear partial differential equation, which can be written as follows:

$$\frac{\partial}{\partial t} \left(\frac{M}{RT} \frac{P_F}{Z} \phi_F \right) - \nabla \cdot \left(\frac{M}{RT} \frac{P_F}{Z} \frac{k_F}{\mu_g} \nabla P_F \right) = 0 \tag{A2.7}$$

By slightly modifying the lift side of Eq. (A2.7) to equal the sign, we obtain:

$$\phi_{F} \frac{P_{F}}{Z(P_{F})} \frac{\partial P_{F}}{\partial t} \left[\frac{1}{P_{F}} - \frac{1}{Z(P_{F})} \frac{\partial Z(P_{F})}{\partial P_{F}} \right] = \nabla \cdot \left[\frac{k_{F}(P_{F})}{\mu(P_{F})} \frac{P_{F}}{Z(P_{F})} \nabla P_{F} \right]$$
(A2.8)

The relationship between the compression coefficient, pressure, and compression factor is given by:

$$C(P_{\rm F}) = \frac{1}{P_{\rm E}} - \frac{1}{Z(P_{\rm E})} \frac{\partial Z(P_{\rm F})}{\partial P_{\rm E}}$$
(A2.9)

Substituting Eq. (A2.9) into Eq. (A2.8) we have

$$\phi_{F} \frac{C(P_{F})P_{F}}{k_{F}(P_{F})Z(P_{F})} \frac{\partial P_{F}}{\partial t} = \nabla \cdot \left[\frac{P_{F}}{\mu(P_{F})Z(P_{F})} \nabla P_{F} \right]$$
(A2.10)

Eq. (A2.10) is a general expression of the unsteady gas percolation equation. We use the complex function derivative rule for the right side of the equal sign of Eq. (A2.10):

$$\phi_F \frac{C(P_F)P_F}{k_F(P_F)Z(P_F)} \frac{\partial P_F}{\partial t} = \frac{P_F}{\mu(P_F)Z(P_F)} \nabla^2 P_F + \frac{d}{dP_F} \left[\frac{P_F}{\mu(P_F)Z(P_F)} \right] (\nabla P_F)^2$$
(A2.11)

Multiplying both sides of Eq. (A2.11) by $\frac{\mu(P_F)Z(P_F)}{P_F}$ we have:

$$\phi_{\mathrm{F}} \frac{\mu(P_{\mathrm{F}})C(P_{\mathrm{F}})}{k_{\mathrm{F}}(P_{\mathrm{F}})} \frac{\partial P_{\mathrm{F}}}{\partial t} = \nabla^{2} P_{\mathrm{F}} + \frac{d}{dP_{\mathrm{F}}} \left[\ln \frac{P_{\mathrm{F}}}{\mu(P_{\mathrm{F}})Z(P_{\mathrm{F}})} \right] (\nabla P_{\mathrm{F}})^{2}$$
(A2.12)

Assuming that the pressure gradient during gas percolation is small, we obtain $(\nabla P_F)^2 \rightarrow 0$ and Eq. (A2.12) becomes:

$$\phi_{\rm F} \frac{\partial P_{\rm F}}{\partial t} = \frac{k_{\rm F}(P_{\rm F})}{\mu(P_{\rm F})C(P_{\rm F})} \nabla^2 P_{\rm F} \tag{A2.13}$$

In this study, we temporarily do not consider the relationship between k_F , u_g , C_F , and P_F drew on the idea of the apparent transport coefficient introduced by Cui et al. (2009) and defined K_F as

$$K_{\rm F} = \frac{k_{\rm F}(P_{\rm F})}{\mu_{\sigma}(P_{\rm F})C_{\rm F}(P_{\rm F})\phi_{\rm F}}$$
 (A2.14)

where K_F is the apparent transport coefficient of the HF region. Substituting Eq. (A2.14) into Eq. (A2.13) we obtain:

$$\phi_{\rm F} \frac{\partial P_{\rm F}}{\partial t} = K_{\rm F} \nabla^2 P_{\rm F} \tag{A2.15}$$

Because the scale of the hydraulic fractures, micro-fractures and macro-pores in the HF region is much larger than the methane molecular diameter, we do not consider the dynamic fractionation of methane molecules in the HF region; that is, $^{12}\text{CH}_4$ and $^{13}\text{CH}_4$ have the same K_F . Therefore, the HF region governing equations for $^{12}\text{CH}_4$ and $^{13}\text{CH}_4$ are as follows:

$$\begin{cases} \phi_{F} \frac{\partial P_{F}}{\partial t} = K_{F} \nabla^{2} P_{F} \\ \phi_{F} \frac{\partial P_{F}^{*}}{\partial t} = K_{F} \nabla^{2} P_{F}^{*} \end{cases}$$
(A2.16)

Appendix B. Calculation of gas production rate, cumulative gas production, $\delta^{13} C_1$, gas ratio, and recovery ratio

B.1. Cumulative gas production

1. HF region:

$$\begin{cases} Q_{\text{cum.free.}^{12}\text{CH}_{4}}^{\text{F}}(t) = \phi_{\text{F}} \times V_{m} \times \iiint_{\text{F}} \frac{P_{\text{F}}(x,y,z,t_{0})}{Z(x,y,z,t_{0})RT} - \frac{P_{\text{F}}(x,y,z,t)}{Z(x,y,z,t)RT} dV \\ Q_{\text{day.free.}^{13}\text{CH}_{4}}^{\text{F}}(t) = \phi_{\text{F}} \times V_{m} \times \iiint_{\text{F}} \frac{P_{\text{F}}^{*}(x,y,z,t_{0})}{Z(x,y,z,t_{0})RT} - \frac{P_{\text{F}}^{*}(x,y,z,t)}{Z(x,y,z,t)RT} dV \\ Q_{\text{cum}}^{\text{F}}(t) = Q_{\text{cum.free.}^{12}\text{CH}_{4}}^{\text{F}}(t) + Q_{\text{day.free.}^{13}\text{CH}_{4}}^{\text{F}}(t) \end{cases}$$
(B1.1)

where $Q_{\text{cum_free_}^{-12}\text{CH}_4}^F$ is the cumulative production of $^{12}\text{CH}_4$ in free gas from the HF region, m^3 ; $Q_{\text{cum_free_}^{-13}\text{CH}_4}^F$ is the cumulative production of $^{13}\text{CH}_4$ in free gas from the HF region, m^3 ; and Q_{cum}^F is the cumulative production in the HF region.

2. SRV region:

$$\begin{cases} Q_{\text{cum_free}_^{12}\text{CH}_{4}}^{I}(t) = \phi_{\text{I}} \times V_{m} \times \iint_{I} \frac{P_{\text{I}}(x, y, z, t_{0})}{Z(x, y, z, t_{0})RT} - \frac{P_{\text{I}}(x, y, z, t)}{Z(x, y, z, t)RT} dV \\ Q_{\text{day_free}_^{13}\text{CH}_{4}}^{I}(t) = \phi_{\text{I}} \times V_{m} \times \iint_{I} \frac{P_{\text{I}}^{*}(x, y, z, t_{0})}{Z(x, y, z, t_{0})RT} - \frac{P_{\text{I}}^{*}(x, y, z, t)}{Z(x, y, z, t)RT} dV \\ Q_{\text{cum_ads}_^{12}\text{CH}_{4}}^{I}(t) = (1 - \phi_{\text{I}}) \times \rho_{\text{rock}} \times V_{L} \times \iint_{I} \theta_{\text{I}}(x, y, z, t_{0}) - \theta_{\text{I}}(x, y, z, t) dV \\ Q_{\text{cum_ads}_^{13}\text{CH}_{4}}^{I}(t) = (1 - \phi_{\text{I}}) \times \rho_{\text{rock}} \times V_{L} \times \iint_{I} \theta_{\text{I}}^{*}(x, y, z, t_{0}) - \theta_{\text{I}}^{*}(x, y, z, t) dV \\ Q_{\text{cum}}^{I}(t) = Q_{\text{cum_free}_^{12}\text{CH}_{4}}^{I}(t) + Q_{\text{day_free}_^{13}\text{CH}_{4}}^{I}(t) + Q_{\text{cum_ads}_^{13}\text{CH}_{4}}^{I}(t) + Q_{\text{cum_ads}_^{13}\text{CH}_{4}}^{I}(t) + Q_{\text{cum_ads}_^{13}\text{CH}_{4}}^{I}(t) \end{cases}$$
(B1.2)

where $Q^{I}_{cum_free_^{12}CH_4}$ is the cumulative production of $^{12}CH_4$ in free gas from the SRV region, m^3 ; $Q^{I}_{cum_free_^{13}CH_4}$ is the cumulative production of $^{13}CH_4$ in free gas from the SRV region, m^3 ; $Q^{I}_{cum_ads_^{12}CH_4}$ is the cumulative production of $^{12}CH_4$ in adsorbed gas from the SRV region, m^3 ; $Q^{I}_{cum_ads_^{13}CH_4}$ is the cumulative production of $^{13}CH_4$ in adsorbed gas from the SRV region, m^3 ; and Q^{I}_{cum} is the cumulative production of the SRV region.

3. USRV region:

$$\begin{cases} Q_{\text{cum_free_}^{12}\text{CH}_{4}}^{O}(t) = \phi_{O} \times V_{\text{m}} \times \iiint_{O} \frac{P_{O}(x,y,z,t_{0})}{Z(x,y,z,t_{0})RT} - \frac{P_{O}(x,y,z,t)}{Z(x,y,z,t)RT} dV \\ Q_{\text{day_free_}^{13}\text{CH}_{4}}^{O}(t) = \phi_{O} \times V_{\text{m}} \times \iiint_{O} \frac{P_{O}^{*}(x,y,z,t_{0})}{Z(x,y,z,t_{0})RT} - \frac{P_{O}^{*}(x,y,z,t)}{Z(x,y,z,t)RT} dV \\ Q_{\text{cum_ads_}^{12}\text{CH}_{4}}^{O}(t) = (1 - \phi_{O}) \times \rho_{\text{rock}} \times V_{L} \times \iiint_{O} \theta_{O}(x,y,z,t_{0}) - \theta_{O}(x,y,z,t) dV \\ Q_{\text{cum_ads_}^{13}\text{CH}_{4}}^{O}(t) = (1 - \phi_{O}) \times \rho_{\text{rock}} \times V_{L} \times \iiint_{O} \theta_{O}^{*}(x,y,z,t_{0}) - \theta_{O}^{*}(x,y,z,t) dV \\ Q_{\text{cum}}^{O}(t) = Q_{\text{cum_free_}^{12}\text{CH}_{4}}^{O}(t) + Q_{\text{day_free_}^{13}\text{CH}_{4}}^{O}(t) + Q_{\text{cum_ads_}^{13}\text{CH}_{4}}^{O}(t) + Q_{\text{cum_ads_}^{13}\text{CH}_{4}^{O}(t) + Q_{\text{cum_ads_}^{13}\text{CH}_{4}^{$$

where the superscript O represents the parameters of the USRV region.

$$\begin{cases} Q_{\text{day_free_}^{12}\text{CH}_{4}}^{\Omega}(t) = \frac{dQ_{\text{cum_free_}^{12}\text{CH}_{4}}^{\Omega}(t)}{dt} \\ Q_{\text{day_ads_}^{12}\text{CH}_{4}}^{\Omega}(t) = \frac{dQ_{\text{cum_ads_}^{12}\text{CH}_{4}}^{\Omega}(t)}{dt} \\ Q_{\text{day_free_}^{13}\text{CH}_{4}}^{\Omega}(t) = \frac{dQ_{\text{cum_free_}^{13}\text{CH}_{4}}^{\Omega}(t)}{dt} \\ Q_{\text{day_ads_}^{13}\text{CH}_{4}}^{\Omega}(t) = \frac{dQ_{\text{cum_ads_}^{13}\text{CH}_{4}}^{\Omega}(t)}{dt} \\ Q_{\text{day}}^{\Omega}(t) = \frac{dQ_{\text{cum}}^{\Omega}(t)}{dt} \end{cases}$$
(B2.1)

B.2. Gas production rate

By calculating the derivative of cumulative gas production over time, it could be done to determine the gas production rate for each region: where Ω is a certain region, which can be the HF region (F), SRV region (I), USRV region (O), or all regions.

B.3. $\delta^{13}C_1$

where V_F , V_I , and V_O are the volumes of the HF, SRV, and USRV regions, respectively, and $P_F(t=0) = P_I(t=0) = P_O(t=0) = P_O(t=0)$ is the initial reservoir pressure).

$$\begin{cases} \delta^{13}C_{1_diffusion}(t) = \left(\frac{Q_{day_free_^{13}CH_4}}{Q_{day_free_^{12}CH_4} \times R_{st}} - 1\right) \times 1000\% \\ \delta^{13}C_{1_adsorption_desorption}(t) = \left(\frac{Q_{day_ads_^{13}CH_4}}{Q_{day_ads_^{12}CH_4} \times R_{st}} - 1\right) \times 1000\% \\ \delta^{13}C_{1}(t)_{-\Omega} = \left[\frac{Q_{day_free_^{13}CH_4}}{Q_{day_free_^{13}CH_4}} + Q_{day_ads_^{13}CH_4}}^{\Omega} - 1\right] \times 1000\% \end{cases}$$
(B3.1)

where $R_{\rm st}$ is the carbon isotope atomic ratio of the PDB standard samples, 0.0112372. The isotope fractionation curve is calculated by subtracting the initial isotope value from the instantaneous isotope value of the produced gas $(\delta^{13}C_1(t)-\delta^{13}C_1\ (t=0))$.

B.4. Gas ratio

$$\begin{cases} \text{ratio}_{\text{_free}} = \frac{Q_{\text{day_free}}(t)}{Q_{\text{day}}(t)} \times 100\% \\ \text{ratio}_{\text{_ads}} = \frac{Q_{\text{day_ads}}(t)}{Q_{\text{ads}}(t)} \times 100\% \\ \text{ratio}_{\text{_}\Omega} = \frac{Q_{\text{day}}^{\Omega}(t)}{Q_{\text{day}}(t)} \times 100\% \end{cases}$$
(B4.1)

B.5. Recovery ratio

$$G_{R_HF} = \frac{\phi_F \cdot P_F(t=0) \cdot V_F}{ZRT} \times V_m$$
 (B5.1)

The reserve of the SRV region is

$$\begin{split} G_{\text{R_inner reservoir}} &= \frac{\phi_{\text{I}} \cdot P_{\text{I}}(t=0) \cdot V_{\text{I}}}{ZRT} \times V_{\text{m}} + (1-\phi_{\text{I}}) \times \rho_{\text{rock}} \\ &\times V_{\text{L}} \times \theta_{\text{I}}(t=0) \times V_{\text{I}} \end{split} \tag{B5.2}$$

The reserve of the USRV region is

$$\begin{split} G_{\text{R_outer reservoir}} &= \frac{\phi_{\text{O}} \cdot P_{\text{O}}(t=0) \cdot V_{\text{O}}}{ZRT} \times V_{\text{m}} + (1 - \phi_{\text{O}}) \times \rho_{\text{rock}} \\ &\times V_{\text{L}} \times \theta_{\text{O}}(t=0) \times V_{\text{O}} \end{split} \tag{B5.3}$$

The recovery ratio is

recovery ratio =
$$\frac{Q_{\text{cum}}(t)}{G_{\text{R_HF}} + G_{\text{R_inner reservoir}} + G_{\text{R_outer reservoir}}} \times 100\%$$
(B5.4)

Appendix C. Validation of the model using previous experimental data

For the reservoir-scale isotope fractionation model, it is challenging to verify the accuracy of its evaluation results. Currently, we can validate the accuracy of our mathematical model to a certain extent using previous experimental data. Gao et al. (2018) conducted a depletion development experiment simulating the full life cycle of a shale gas well. The experiment's general procedure involved placing a full-diameter shale core into a holder, applying confining pressure around the core, injecting methane for saturation, and then restoring it to the original reservoir pressure. Afterward, the outlet valve was opened to simulate the gas well production process (Fig. C1(a)). The mathematical model developed in Section 2 of this study was applied to the experimental process to perform numerical simulations of the depletion process of the fulldiameter core, solving for the core's internal pressure field (Fig. C1(b)). By integrating the pressure field to calculate cumulative gas production, inlet pressure, and production rate, and performing history matching with experimental data, it was evident that the CIF model achieved a good fit with the experimental data for cumulative production, inlet pressure, and production rate (Fig. C2(a), (b) and (c)). The porosity obtained through history matching and inversion calculation was 1.22%, which is close to the result of 1.13% calculated by previous researchers using the material balance method (Fig. C2(d)). This partially validated the reliability of the model. In the future, we will conduct isotope fractionation simulation experiments for the full life cycle of shale gas wells to further validate the established model.

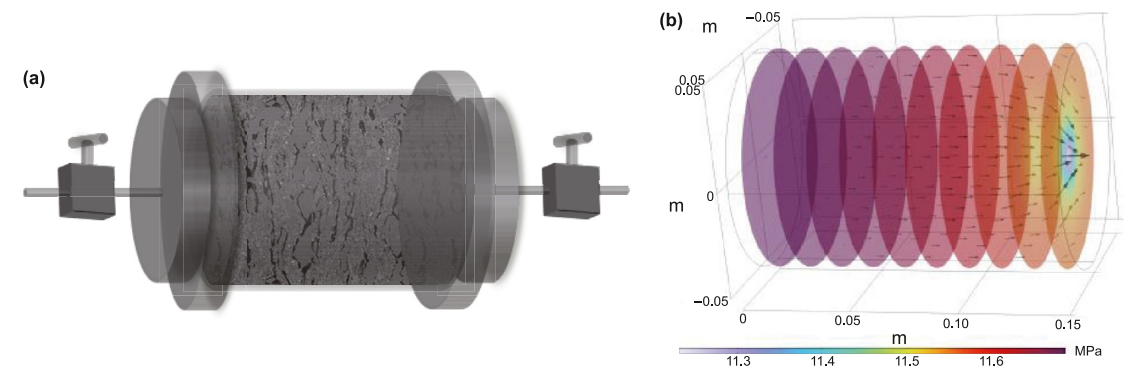


Fig. C1. Schematic diagram of depletion development of full diameter core and pressure field distribution calculated by CIF model.

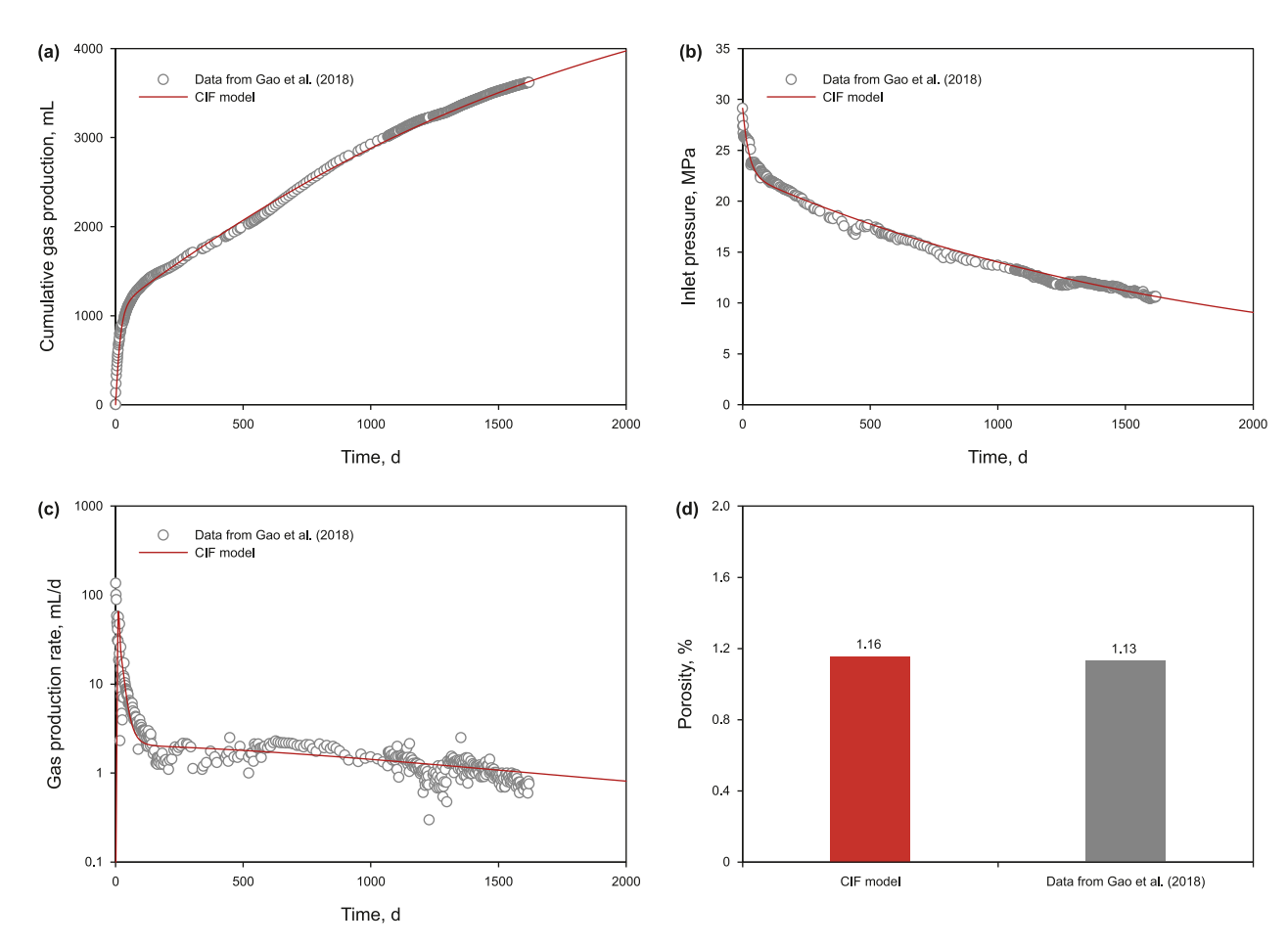


Fig. C2. The history matching of Gao et al.'s experimental data and the inversion porosity by model were compared with experimental results. Parameters: $P_0 = 29.13$ MPa; $\rho_{\text{rock}} = 2.6 \text{ g/cm}^3; D_{\text{ma}} = 7.83 \times 10^{-10} \text{ m}^3/\text{s}; D_{\text{mi}} = 3.07 \times 10^{-11} \text{ m}^3/\text{s}; \phi_{\text{mi}} = 1.16\%; \phi_{\text{ma}} = 0.36 \%; T = 25 \text{ °C}; P_{\text{L}} = 1.02 \text{ MPa}; V_{\text{L}} = 2.1926 \text{ cm}^3/\text{g}; r_{\text{core}} = 5 \text{ cm}; H = 15 \text{ cm}.$

References

Al-Ahmadi, H.A., Wattenbarger, R.A., 2011. Triple-porosity models: one further step towards capturing fractured reservoirs heterogeneity. In: SPE/DGS Saudi Arabia Section Technical Symposium and Exhibition. https://doi.org/10.2118/149054-

Arps, J.J., 1945. Analysis of decline curves. Transactions of the AIME 160 (1),

228-247. https://doi.org/10.2118/945228-G.
Bello, R.O., Wattenbarger, R.A., 2010. Multi-stage hydraulically fractured shale gas rate transient analysis. In: North Africa Technical Conference and Exhibition, Cairo, Egypt. https://doi.org/10.2118/126754-MS

Bird, R., Stewart, W., Lightfoot, E., 2002. Transport Phenomena. New York.

Brown, M., Ozkan, E., Raghavan, R., et al., 2011. Practical solutions for pressuretransient responses of fractured horizontal wells in unconventional shale reservoirs. SPE Reservoir Eval. Eng. 14 (6), 663-676. https://doi.org/10.2118/ 125043-PA.

Bruner, F., Cartoni, G.P., Liberti, A., 1966. Gas chromatography of isotopic molecules on open tubular columns. Anal. Chem. 38 (2), 298–303. https://doi.org/10.1021/ ac60234a035.

Cao, P., Liu, J., Leong, Y.-K., 2016. A fully coupled multiscale shale deformation-gas transport model for the evaluation of shale gas extraction. Fuel 178, 103-117. https://doi.org/10.1016/j.fuel.2016.03.055.

Chen, F., Jiang, C., Shi, P., et al., 2016. Geochemical characteristics of terrestrial shale gas and its production prediction significance in the Ordos Basin, China. Journal Geoscience 1 (6), 425-433. https://doi.org/10.1016/ of Natural Gas j.jnggs.2016.11.007.

Ci, X., Zhang, L., Niu, Q., et al., 2019. Application of carbon isotope logging technology in shale gas exploration and development. In: International Field

Exploration and Development Conference 2019, pp. 413–424 (in Chinese). http://10.26914/c.cnkihy.2019.050131.

- Clark, A.J., Lake, L.W., Patzek, T.W., 2011. Production forecasting with logistic growth models. In: SPE Annual Technical Conference and Exhibition, Denver, Colorado, USA. https://doi.org/10.2118/144790-MS.
- Cui, X., Bustin, A.M.M., Bustin, R.M., 2009. Measurements of gas permeability and diffusivity of tight reservoir rocks: different approaches and their applications. Geofluids 9 (3), 208–223. https://doi.org/10.1111/j.1468-8123.2009.00244.x.
- Curtis, J.B., 2002. Fractured shale-gas systems. AAPG (Am. Assoc. Pet. Geol.) Bull. 86 (11), 1921–1938. https://doi.org/10.1306/61EEDDBE-173E-11D7-8645000102C1865D.
- Duong, A.N., 2010. An unconventional rate decline approach for tight and fracture-dominated gas wells. In: Canadian Unconventional Resources and International Petroleum Conference. Calgary, Alberta, Canada, SPE-137748-MS. http://10.2118/137748-MS.
- Fang, Y., 2017. Research on the Law of Single Well Production Decline in JY Shale Gas Reservoir. Southwest University of Petroleum (in Chinese).
- Gao, L., Wu, S., Deev, A., et al., 2017. The gas isotope interpretation tool: a novel method to better predict production decline. AAPG (Am. Assoc. Pet. Geol.) Bull. 101 (8), 1263–1275. http://10.1306/09221615106.
- Gao, S., Liu, H., Ye, L., et al., 2018. Physical simulation experiment and numerical inversion of the full life cycle of shale gas well. Acta Pet. Sin. 39 (4), 435–444 (in Chinese). http://10.7623/syxb201804007.
- Ge, Z., Li, S., Zhou, Z., et al., 2018. Modeling and experiment on permeability of coal with hydraulic fracturing by stimulated reservoir volume. Rock Mech. Rock Eng. 52 (8), 2605–2615. http://10.1007/s00603-018-1682-z.
- Han, Y., Fan, M., Shen, B., et al., 2017. The geochemical characteristics and significance of desorption gas in organic-enriched shale. Nat. Gas Geosci. 28 (7), 1065–1071 (in Chinese). http://10.11764/j.issn.1672-1926.2017.01.001.
- Ho, C., Webb, S., 2006. Gas Transport in Porous Media. Springer, Netherlands.
- Hu, Z., Duan, X., Shao, N., et al., 2021. Experimental study on the characteristics of adsorbed gas and gas production in shale formations. Geofluids 2021, 1–12. http://10.1155/2021/2448044.
- Hu, Y., Liu, G., Luo, N., et al., 2022. Multi-field coupling deformation of rock and multi-scale flow of gas in shale gas extraction. Energy 238, 121666. http://10. 1016/j.energy.2021.121666.
- Ilk, D., Rushing, J.A., Perego, A.D., et al., 2008. Exponential vs. hyperbolic decline in tight gas sands — understanding the origin and implications for reserve estimates using Arps' decline curves. In: PE Annual Technical Conference and Exhibition. Denver, Colorado, USA. http://10.2118/116731-MS.
- International Energy Agency (IEA), 2016. Shale gas production drives world natural gas production growth. Today in Energy [EB/OL]. https://www.eia.gov/todayinenergy/detail.php?id=27512.
- Jiang, R., Zhang, F., Cui, Y., et al., 2019. Production performance analysis of fractured vertical wells with SRV in triple media gas reservoirs using elliptical flow. J. Nat. Gas Sci. Eng. 68, 102925. http://10.1016/j.jngse.2019.102925.
- Kang, J., Fu, X., Liang, S., et al., 2019. A numerical simulation study on the characteristics of the gas production profile and its formation mechanisms for different dip angles in coal reservoirs. J. Petrol. Sci. Eng. 181, 106198. http://10.1016/j.petrol.2019.106198.
- Lee, W.J., Sidle, R.E., 2010. Gas reserves estimation in resource plays. J Pet Technol 62 (12), 65–67. http://10.2118/130102-MS.
- Li, X., Zhang, D., Li, S., 2015. A multi-continuum multiple flow mechanism simulator for unconventional oil and gas recovery. J. Nat. Gas Sci. Eng. 26, 652–669. http://10.1016/ji.jngse.2015.07.005.
- Li, W., Lu, S., Li, J., et al., 2020a. Carbon isotope fractionation during shale gas transport: mechanism, characterization and significance. Sci. China Earth Sci. 63 (5), 674–689. http://10.1007/s11430-019-9553-5.
- Li, W., Lu, S., Li, J., et al., 2021. Geochemical modeling of carbon isotope fractionation during methane transport in tight sedimentary rocks. Chem. Geol. 566. http:// 10.1016/j.chemgeo.2020.120033.
- Li, W., Li, X., Zhao, S., et al., 2022a. Evaluation on carbon isotope fractionation and gas-in-place content based on pressure-holding coring technique. Fuel 315, 123243. http://10.1016/j.fuel.2022.123243.
- Li, Y., 2020b. Multi-scale Flow Mechanism Analysis and Productivity Evaluation of Shale Gas. China University of Petroleum, Beijing (in Chinese).
- Li, W., Li, J., Lu, S., et al., 2022b. Evaluation of gas-in-place content and gas-adsorbed ratio using carbon isotope fractionation model: a case study from Longmaxi shales in Sichuan Basin, China. Int. J. Coal Geol. 249, 103881. https://doi.org/10.1016/j.coal.2021.103881.
- Li, W., Lu, S., Li, J., et al., 2022c. Research progress on isotopic fractionation in the process of shale gas/coalbed methane migration. Petrol. Explor. Dev. 49 (5), 1069–1084. http://10.1016/S1876-3804(22)60333-1.
- Liu, Z, Chen, D, Zhang, J, Lv, X, Dang, W, Liu, Y, et al., 2019. Combining Isotopic Geochemical Data and Logging Data to Predict the Range of the Total Gas Content in Shale: A Case Study from the Wufeng and Longmaxi Shales in the Middle Yangtze Area. South China. http://10.1021/acs.energyfuels.9b01879.
- Liu, Y, Zhang, J, Tang, X, 2016. Predicting the proportion of free and adsorbed gas by isotopic geochemical data: A case study from lower Permian shale in the southern North China basin (SNCB). Int. J. Coal Geol. 156, 25—35. https://doi.org/ 10.1016/j.coal.2016.01.011.

- Luo, H., Liu, W., Fan, M., et al., 2019. New way of predicting production state by carbon isotope fractionation in the fuling shale gas field, Southeast Sichuan Basin. Acta Geol. Sin. 93 (2), 491–492. http://10.1111/1755-6724.13837.
- Ma, Y., Zhong, N., Yao, L., et al., 2020. Shale gas desorption behavior and carbon isotopic variations of gases from canister desorption of two sets of gas shales in south China. Mar. Petrol. Geol. 113, 104127. http://10.1016/j.marpetgeo.2019.
- Micheal, M., Yu, H., Meng, S., et al., 2023. Gas production from shale reservoirs with bifurcating fractures: a modified quadruple-domain model coupling microseismic events. Energy 278, 127780. http://10.1016/j.energy.2023.127780.
- Mishra, S., 2012. A new approach to reserves estimation in shale gas reservoirs using multiple decline curve analysis models. All Days. SPE. http://10.2118/161092-MS.
- Nie, B., 2023. Diffusion characteristics of shale mixed gases on the wall of microscale fractures. Energy 284, 128405. https://doi.org/10.1016/j.energy.2023.128405.
- Niemann, M., Whiticar, M.J., 2017. Stable isotope systematics of coalbed gas during desorption and production. Geosciences 7, 43. http://10.3390/geosciences7020043.
- Niu, Q., Zhang, H., Zhu, D., et al., 2020. Mud gas isotopic logging of Wufeng-Longmaxi shale in southeastern Sichuan Basin. Nat. Gas Geosci. 31 (3), 1294–1305. http://10.11764/j.issn.1672-1926.2020.05.008.
- Ozkan, E., Brown, M., Raghavan, R., et al., 2011. Comparison of fractured-horizontalwell performance in tight sand and shale reservoirs. SPE Reservoir Eval. Eng. 14 (2), 248–259. http://10.2118/121290-PA.
- Stalgorova, E., Mattar, L., 2012. Practical analytical model to simulate production of horizontal wells with branch fractures. In: SPE Canadian Unconventional Resources Conference, Calgary, Alberta, Canada. http://10.2118/162515-MS.
- Tao, C., Zhai, C., Yu, L., et al., 2020. Carbon isotope fractionation characteristics during shale gas release. Petroleum Geology Experiment 42 (1), 113–116 (in Chinese). http://10.11781/sysydz202001113.
- Tian, Y., Ju, B., 2016. A model for predicting shale gas production decline based on the BP neural network improved by the genetic algorithm. China Sciencepaper 11 (15), 1710–1715 (in Chinese). http://2095-2783(2016)15-1710-06.
- 11 (15), 1710—1715 (in Chinese). http://2095-2783(2016)15-1710-06.

 Tivayanonda, V., Apiwathanasorn, S., Ehlig-Economides, C., et al., 2012. Alternative Interpretations of shale gas/oil rate behavior using a triple porosity model. In: SPE Annual Technical Conference and Exhibition, San Antonio, Texas, USA. http://10.2118/159703-MS.
- Valkó, P.P., Lee, W.J., 2010. A better way to forecast production from unconventional gas wells. In: SPE Annual Technical Conference and Exhibition. https://doi.org/ 10.2118/134231-MS. Florence, Italy.
- Wang, J.G., Hu, B., Liu, H., et al., 2018. Effects of 'soft-hard' compaction and multiscale flow on the shale gas production from a multistage hydraulic fractured horizontal well. J. Petrol. Sci. Eng. 170, 873—887. http://10.1016/j.petrol.2018.07. 012.
- Wang, W., Fan, D., Sheng, G., et al., 2019. A review of analytical and semi-analytical fluid flow models for ultra-tight hydrocarbon reservoirs. Fue 256, 115737. http://10.1016/j.fuel.2019.115737.
- Wei, Y., Lu, S., Li, J., et al., 2021. Impacts of gas pressure on carbon isotope fractionation during methane degassing—an experimental study on shales from Wufeng and Longmaxi Formations in southeast Sichuan, China. Mar. Petrol. Geol. 128, 105001. http://10.1016/j.marpetgeo.2021.105001.
- Wu, J., Di, Y., Zhang, J., et al., 2021. Numerical simulation research on influencing factors of post-fracturing flowback of shale gas wells in the Sichuan Basin. Front. Earth Sci. 9. http://10.3389/feart.2021.745393.
- Xia, X., Tang, Y., 2012. Isotope fractionation of methane during natural gas flow with coupled diffusion and adsorption/desorption. Geochem. Cosmochim. Acta 77, 489–503. http://10.1016/j.gca.2011.10.014.
- Xue, D., Chen, Z., Lu, C., 2022. Establishment of the comprehensive material balance equation for coalbed methane reservoirs at the gas desorption stage. Fuel 326, 124979. http://10.1016/j.fuel.2022.124979.
- Yan, X., Wang, X., Zhang, H., et al., 2015. Analysis of sensitive parameter in numerical simulation of shale gas reservoir with hydraulic fractures. Journal of Southwest Petroleum University (Science & Technology Edition) 37 (6), 127–132 (in Chinese). http://10.11885/j.issn.1674-5086.2013.06.14.04.
- Yu, R., Jiang, W., Zhang, X.W., et al., 2018. A review of empirical production decline analysis methods for shale gas reservoir. China Petroleum Exploration 23 (1), 109–116 (in Chinese). http://10.3969/j.issn.1672-7703.2018.01.012.
- Zhang, T., Krooss, B.M., 2001. Experimental investigation on the carbon isotope fractionation of methane during gas migration by diffusion through sedimentary rocks at elevated temperature and pressure. Geochem. Cosmochim. Acta 65 (16), 2723–2742. http://10.1016/S0016-7037(01)00601-9.
- Zhang, L., Gao, J., Hu, S., et al., 2016. Five-region flow model for MFHWs in dual porous shale gas reservoirs. J. Nat. Gas Sci. Eng. 33, 1316–1323. http://10.1016/j.ingse 2016 05 063
- Zhang, M., Tang, Q., Cao, C., et al., 2018. Molecular and carbon isotopic variation in 3.5 years shale gas production from Longmaxi Formation in Sichuan Basin, China. Mar. Petrol. Geol. 89, 27–37. https://doi.org/10.1016/j.marpetgeo.2017.01.023.
- Zhao, S., Kang, S., Zheng, M., et al., 2022. Prediction of decline in shale gas well production using stable carbon isotope technique. Front. Earth Sci. 15 (4), 849–859. http://10.1007/s11707-021-0935-4.

- Zhao, Y, Lu, G, Zhang, L, Wei, Y, Guo, J, Chang, C, 2020. Numerical simulation of shale gas reservoirs considering discrete fracture network using a coupled multiple transport mechanisms and geomechanics model. J. Petrol. Sci. Eng. 195, 107588. https://doi.org/10.1016/j.petrol.2020.107588.
- Zhao, S., Yang, X., Liu, Y., et al., 2024. Characteristics and geological implications of carbon isotope fractionation during deep shale gas production: a case study of
- the Ordovician Wufeng FormationSilurian Longmaxi Formation in the Luzhou Block of Southern Sichuan Basin. Nat. Gas. Ind. 44 (8), 72–84 (in Chinese). http://10.3787/j.issn.1000-0976.2024.08.006.
- Zheng, J., Ju, Y., Liu, H.H., et al., 2016. Numerical prediction of the decline of the shale gas production rate with considering the geomechanical effects based on the two-part Hooke's model. Fuel 185, 362–369. http://10.1016/j.fuel.2016.07.112.